

**DPGIIL: Dirichlet Process-Deep Generative Model-Integrated Incremental
Learning for Clustering in Transmissibility-based Online Structural Anomaly
Detection**

Lin-Feng Mei¹, Wang-Ji Yan^{1,2*}

*¹State Key Laboratory of Internet of Things for Smart City and Department of Civil and
Environmental Engineering, University of Macau, China*

²Guangdong-Hong Kong-Macau Joint Laboratory for Smart Cities, China

Abstract: Clustering based on vibration responses, such as transmissibility functions (TFs), is promising in structural anomaly detection, but most existing approaches struggle with determining the optimal cluster number and handling high-dimensional streaming data, while their shallow structures also make them sensitive to manually-engineered feature quality. To bridge this gap, this work proposes the Dirichlet process-deep generative model-integrated incremental learning (DPGIIL) for clustering by combining the advantages of deep generative models (DGMs) in representation learning and the Dirichlet process mixture model (DPMM) in identifying distinct patterns in observed data. By introducing a DPMM prior into the latent space of DGMs, DPGIIL automatically captures dissimilarities in extracted latent representations, enabling both generative modeling and clustering. Within the context of variational Bayesian inference, a lower bound on the log marginal likelihood of DPGIIL, tighter than the evidence lower bound given sufficient training data, is derived analytically, which enables the joint optimization of DGM and DPMM parameters, thereby allowing the DPMM to regularize the DGM’s feature extraction process. Additionally, a greedy

split-merge scheme-based coordinate ascent variational inference method is devised to accelerate the optimization. The summary statistics of the DPMM, along with the network parameters, are used to retain information about previous data for incremental learning. Notably, this study uses variational autoencoder (VAE) within DPGIIL as an illustrative example, while this framework is adaptable to other DGMs. Two case studies show that the proposed method outperforms some state-of-the-art approaches in structural anomaly detection and clustering, while also dynamically generating new clusters to indicate the emergence of new structural conditions for online monitoring.

Keywords: Dirichlet process mixture models; Deep generative models; Incremental learning; Online structural anomaly detection.

*Corresponding author.

E-mail address: yc17409@um.edu.mo (L.F. Mei); wangjiyan@um.edu.mo (W.J. Yan)

1 Introduction

The service life of engineering structures inevitably decreases during long-term operation, which underscores the significance of ensuring their operating safety to prevent unexpected monetary losses and casualties. In recent years, with the rapid development of sensor systems, computing resources, and data processing approaches, vibration-based structural health monitoring (SHM) with machine learning (ML) techniques has become one of the most prevalent methods to ensure structural safety [1-3], which mainly includes unsupervised and supervised methods according to the employed ML techniques. Unsupervised methods are more flexible as they require only labels of normal condition data [1]. However, they are mainly used for fundamental tasks, predominately structural anomaly detection, due to the lack of information about different damage patterns. In contrast, supervised methods can handle higher-level tasks such as damage classification and quantification, but are often limited by the high cost of obtaining well-annotated training data from various damage scenarios [4].

Currently, outlier analysis-based methods have been widely used for structural anomaly detection, which establishes a baseline based on training data from normal conditions, and any deviation from this baseline is identified as a structural anomaly caused by damage [1]. A pivotal milestone in this area was proposed by Worden et al. [5], in which they employed the Mahalanobis squared distance (MSD) of transmissibility functions (TFs) as the damage index and established a statistical threshold based on Monte Carlo simulation to identify structural anomalies. This approach has since been followed and refined in numerous studies [6-9]. Recently, with

the growing dominance of deep learning (DL) in modern ML, various DL models have been modified and applied to vibration-based SHM [10-12]. In outlier analysis-based structural anomaly detection, deep generative model (DGM)-based approaches have gained popularity due to their unsupervised nature [13]. These methods utilize DGMs to model a complex, high-dimensional baseline distribution from training data to represent normal conditions, with deviations from this baseline indicating the existence of damage. Compared to shallow learning-based methods, DGMs generally perform better to capture the complex statistical properties of training data owing to the exceptional nonlinear mapping capability of deep neural networks [14]. Additionally, DGMs can be flexibly applied in supervised or semi-supervised learning given labeled training data, as they can extract representative features from raw structural response measurements [15]. Furthermore, leveraging the learned probability distributions, DGMs can be used for data augmentation to address the common challenge of limited training data in vibration-based SHM [16, 17]. Utilizing the physical properties of long-gauge static strain TF, Liu et al. [18] proposed an element-wise structural anomaly detection method using paralleled variational autoencoders (VAEs), which can also be used for damage quantification given labeled training data. Inspired by the representation learning capability of VAEs, Ma et al. [14] developed a VAE-based structural anomaly detection method, which combines a moving window with damage-sensitive features automatically extracted by a VAE to detect structural anomalies. Luo et al. [19] introduced an improved generative adversarial network (GAN) to extract latent representations from raw data, integrating it with cloud model theory to reduce

damage misjudgment and enhance the robustness of structural anomaly detection.

Despite these achievements, outlier analysis-based methods are limited to distinguishing between healthy and damaged states, making them sensitive to threshold establishment and unable to provide additional information about the operating conditions of the monitored structure [20, 21]. However, such information is crucial for identifying different patterns of structural behavior and guiding decision-makers in determining further treatments for detected structural anomalies [20, 21]. Clustering is a promising approach to counteract this limitation, which partitions the dataset into distinct groups based on the inherent similarity of data points to indicate different patterns of structural behavior. Over the years, various clustering-based methods, such as K-means clustering [22, 23], hierarchical clustering [24, 25], density-based clustering [26], and Gaussian mixture model (GMM) clustering [27, 28], have been proposed and applied to vibration-based structural anomaly detection and health monitoring, which demonstrate the feasibility and effectiveness of clustering in this field. However, most of these methods require the number of clusters prespecified [24], but there is no standard method to determine the optimal cluster number [29]. Additionally, most existing methods lack incremental learning capability, which refers to the ability to process new data in real-time without forgetting previously learned information [30] and is demanded for practical structural anomaly detection systems. To address these issues, Bayesian nonparametric mixture models have been introduced in this field [20, 21], which employ a nonparametric prior to dynamically adapt the cluster number based on observed data while enabling incremental learning by updating

the posterior with new observations. However, these approaches rely on shallow learning, limiting their capability to handle high-dimensional, highly nonlinear raw structural responses. Therefore, they require a manual feature selection process for dimensionality reduction [20, 21], making their performance sensitive to the quality of these manually-engineered structural features.

In light of the aforementioned issues and challenges, this work proposes a deep clustering framework that combines DGMs with Bayesian nonparametric mixture models. While this work uses the VAE in this framework as an illustrative example, it can be flexibly generalized to other DGMs, such as flow-based models [31]. Although DGM-based clustering is not yet widely used in vibration-based structural anomaly detection, it has gained attention in recent years. Some studies [32-35] integrate GMMs into DGMs to utilize the mixture model as a prior in latent space for enhancing information capacity, while the DGMs' powerful representation learning and reconstruction capabilities overcome the limitations of traditional GMMs in capturing nonlinearity due to their shallow structure [36]. To address the need for prespecifying cluster number, Nalisnick and Smyth [37] introduced the stick-breaking VAE by replacing the prior of vanilla VAE with a stick-breaking process. While this method effectively learns discriminative latent representations for clustering, it lacks detailed information about individual cluster shapes and densities. Bing et al. [38] proposed a deep clustering method by integrating memoized online variational inference-based Dirichlet process mixture models (DPMMs) [39] into the VAE framework. Despite its good clustering performance, this method lacks a generative process for latent

representations and a mathematically rigorous analysis of the loss function. Different from existing approaches, this work introduces a novel DGM-based clustering framework, referred to as Dirichlet process-deep generative model-integrated incremental learning (DPGIIL) for clustering, and applies it to online structural anomaly detection. The major contributions of this work are summarized as follows:

- A deep clustering framework is developed for online structural anomaly detection by integrating the DPMM and DGM, which leverages the representation learning capability of DGMs to avoid manual feature selection required in traditional DPMM-based clustering, combined with the DPMM’s advantage in adaptively identifying distinct patterns in observed data. The Dirichlet process-variational autoencoder-integrated incremental learning (DPVIL) for clustering serves as an illustrative example in this work, while this framework is adaptable to other DGMs.
- A lower bound on the log marginal likelihood of DPVIL, tighter than the evidence lower bound given sufficient training data, is derived to enable the joint optimization of both DPMM and network parameters through an iterative approach. This method allows the DPMM to regularize the feature extraction process of the VAE, while the latent representations concurrently influence the clusters identified by the DPMM. Consequently, DPVIL enables dynamically adjusting the number, density, and shape of clusters in the latent space of the VAE based on observed data.
- By storing the summary statistics of the DPMM, as well as the network parameters, DPVIL enables adapting the identified clusters within an incremental learning context to maintain a high level of clustering performance, making it well-suited

for online structural anomaly detection.

2 Preliminaries

In this section, some key concepts of Bayesian nonparametric mixture models and the VAE are provided, which form the theoretical foundation of the proposed deep clustering framework. Additionally, the rationale for applying this framework to TF-based online structural anomaly detection is illustrated.

2.1 Dirichlet process mixture models

2.1.1 Fundamentals of the DPMM

The DPMM is a Bayesian nonparametric mixture model used for density estimation and clustering, which employs the Dirichlet process (DP) as a nonparametric prior to encompass both the component number and the parameters of each component. The DP is a stochastic process parameterized by a concentration parameter α and a base distribution H . Each sample of a DP is a discrete distribution whose marginal distributions are Dirichlet distributed [40]. For the DPMM, the DP is used as a nonparametric prior in a hierarchical Bayesian specification, with the explicit realization achieved through the stick-breaking representation [41]: In each step, a random variable v_k is drawn from the beta distribution $\text{Beta}(1, \alpha)$, and the mixing proportion of each component is $\pi_k(v) = v_k \prod_{i=1}^{k-1} (1 - v_i)$. This can be metaphorically interpreted as successively breaking a unit length stick into infinite segments, as shown in Fig. 1 [40]. Subsequently, the parameters of each component η_k are drawn from the base distribution H , while the generative process of an observation x_n is determined by these parameters and an assignment variable c_i drawn from the categorical

distribution $\text{Cat}(\pi_k(v))$, i.e., $x_n \sim F(x_n | \eta_{c_n})$. For more details of the DPMM, one can refer to [40, 41].

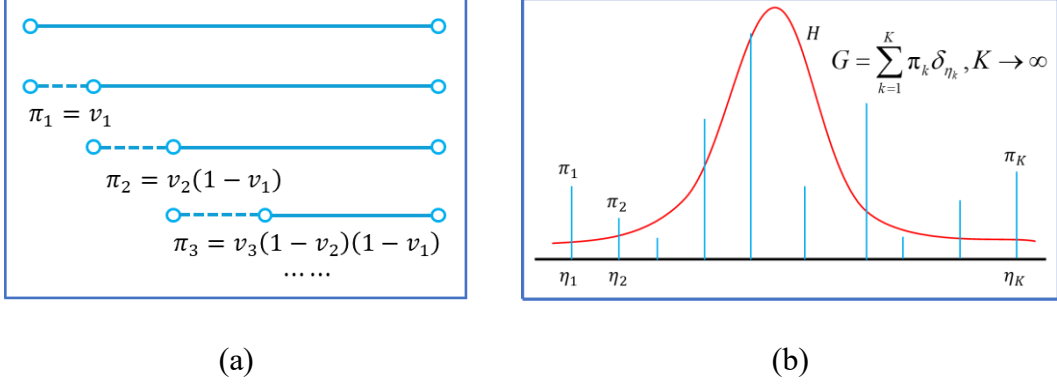


Figure 1. Schematic illustration of (a) the stick-breaking representation and (b) a sample drawn from a Dirichlet process.

2.1.2 CAVI for the DPMM

Like many other Bayesian approaches, explicit inference for the true posterior distribution under a DPMM prior is challenging, which motivates the development of CAVI-based methods [20, 39, 41, 42] to approximate the true posterior. These methods use the conjugate prior of component parameters as the base distribution, combined with a fully factorized variational distribution, to iteratively optimize each factor. In this work, the truncation-free VI-DPGMM [20] is followed as it explicitly accounts for inactive components (those without assigned data) in the DPMM to provide a more reasonable criterion for adding new active components to the variational distribution.

Assuming the base distribution is $H(\eta|\varphi)$, the posterior can be expressed as:

$$\begin{aligned}
 p(v, c, \eta | X, \varpi) &= \frac{p(v, c, \eta | \varpi) p(X | v, c, \eta)}{p(X | \varpi)} \\
 &= \frac{\prod_{k=1}^{\infty} \text{Beta}(v_k | 1, \alpha) H(\eta_k | \varphi) \prod_{n=1}^N \text{Cat}(c_n | v) F(x_n | \eta_{c_n})}{p(X | \varpi)} \quad (1)
 \end{aligned}$$

where $X = \{x_1, x_2, \dots, x_N\}$ is observed data; $\varpi = \{\alpha, \varphi\}$ denotes the hyperparameters. both $F(\cdot)$ and $H(\cdot)$ belong to the exponential family. In terms of VI, a variational distribution $q(v, c, \eta | \hat{\varpi})$ is introduced to approximate the true posterior by minimizing the Kullback-Leibler (KL) divergence between them, which is equivalent to maximizing the evidence lower bound (ELBO) $\mathcal{L}(\hat{\varpi})$ given as [20]:

$$\mathcal{L}(\hat{\varpi}) = \mathbb{E}_q \left[\log p(X, v, c, \eta | \varpi) \right] - \mathbb{E}_q \left[\log q(v, c, \eta | \hat{\varpi}) \right] \quad (2)$$

Based on the mean-field assumption, a fully factorized variational distribution $q(v, c, \eta | \hat{\varpi}) = \prod_{k=1}^{\infty} q(v_k | \hat{\alpha}_k) \prod_{k=1}^{\infty} q(\eta_k | \hat{\varphi}_k) \prod_{n=1}^N q(c_n | \hat{\pi}_n)$ is used, where $\hat{\varpi} = \{\hat{\alpha}, \hat{\varphi}, \hat{\pi}\}$ denotes the variational parameters and $q(v_k | \hat{\alpha}_k) = \text{Beta}(v_k | \hat{\alpha}_{k1}, \hat{\alpha}_{k2})$, $q(\eta_k | \hat{\varphi}_k) = H(\eta_k | \hat{\varphi}_k)$, $q(c_n | \hat{\pi}_n) = \text{Cat}(c_n | \hat{\pi}_{n1}, \hat{\pi}_{n2}, \dots, \hat{\pi}_{nK})$. To handle the infinite components in the DPMM, [20] introduced a truncation-free VI-based DPMM by setting the variational distributions of the parameters for inactive components as their corresponding priors. Based on this assumption, the sum of the probabilities for a data point to be assigned to these inactive components can be analytically derived:

$$\sum_{k=K_a+1}^{\infty} \hat{\pi}_{nk} = \frac{\sum_{k=K_a+1}^{\infty} \hat{\rho}_{nk}}{\sum_{j=1}^{K_a} \hat{\rho}_{nj} + \sum_{j=K_a+1}^{\infty} \hat{\rho}_{nj}}; \quad \sum_{k=K_a+1}^{\infty} \hat{\rho}_{nk} = \frac{\hat{\rho}_{n(K_a+1)}}{1 - \exp\{\psi(\alpha) - \psi(1 + \alpha)\}} \quad (3)$$

where K_a is the number of active components; $\hat{\rho}_{nk}$ is the unnormalized form of $\hat{\pi}_{nk}$. Given the updated $\hat{\pi}_{nk}$, the other variational parameters, $\hat{\alpha}_k$ and $\hat{\varphi}_k$, can also be optimized using the coordinate ascent algorithm [41], and the ELBO is given by:

$$\mathcal{L}(\hat{\varpi}) = \sum_{k=1}^{K_a} \left(\mathbb{E}_q \left[\log \frac{p(v_k | \alpha)}{q(v_k | \hat{\alpha}_k)} \right] + \mathbb{E}_q \left[\log \frac{p(\eta_k | \varphi)}{q(\eta_k | \hat{\varphi}_k)} \right] \right) + \sum_n \log \sum_{k=1}^{\infty} \hat{\rho}_{nk} \quad (4)$$

The sum of probabilities $\sum_{k=K_a+1}^{\infty} \hat{\pi}_{nk}$ then serves as the criterion to activate new components [20], allowing this method to dynamically adjust the component number to adapt to observed data. For more details about this algorithm, one can refer to [20].

Despite the advantages of the truncation-free VI-DPGMM, it struggles with high-dimensional complex data due to its shallow learning nature, making it sensitive to the quality of manually-engineered low-dimensional structural features when employed in structural anomaly detection. To address this issue, this work integrates this method into the DGM framework, allowing for simultaneously extracting latent representations from raw dynamic responses for dimensionality reduction and clustering to indicate different structural conditions. This approach is implemented using a VAE as an illustrative example, while can also be generalized to other DGMs.

2.2 Variational autoencoders

The variational autoencoder [43], illustrated in [Fig. 2](#), is one of the most prevalent DGMs, which connects a neural network (encoder) to another one (decoder) through a probabilistic latent space. The latent space is typically modeled as a diagonal Gaussian distribution that corresponds to the parameters of a variational distribution. Despite its strong performance in probabilistic modeling and feature extraction, the vanilla Gaussian VAE struggles to learn discriminative representations from raw data, as the latent representation for each sample is modeled with a distinct distribution, limiting its ability to capture shared structures within the dataset [32]. This limitation restricts the primary application of vanilla VAEs in structural anomaly detection to outlier analysis-based methods, which are sensitive to the threshold and fail to provide additional

information about the operating conditions of the monitored structure. To address this issue, this work introduces a DPMM prior into the latent space of vanilla VAEs to form DPVIL, which enables extracting discriminative representations from raw dynamic responses for clustering-based structural anomaly detection.

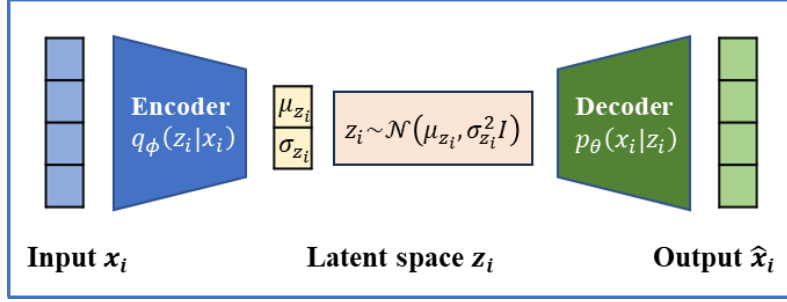


Figure 2. Schematic diagram of a vanilla VAE.

2.3 Rationale of DPVIL for clustering in TF-based online structural anomaly detection

By integrating the DPMM with the VAE, DPVIL automatically extracts low-dimensional discriminative representations from raw data and partitions them into clusters. This approach is used for structural anomaly detection with TF measurements in this work, aiming to leverage the sensitivity of TFs to structural damage and their robustness to excitation [27]. Additionally, it enables incorporating comprehensive frequency domain information by utilizing TF vectors over a wide frequency band [27], while avoiding the need for dimensionality reduction through manual feature selection. During the training phase, labeled data from healthy states, known a priori in structural anomaly detection, are used to identify clusters denoting normal operating conditions. In the subsequent monitoring phase, DPVIL is incrementally updated with new TF measurements, while anomaly detection is performed by determining whether a new

sample belongs to one of the clusters representing normal conditions, as described in [20]. Compared to existing approaches, this method automatically extracts discriminative representations from raw TF vectors to integrate comprehensive frequency domain information without requiring manual feature selection. It also generates clusters to indicate different structural conditions, providing more information than merely distinguishing between “healthy” and “damaged” states. Moreover, DPVIL is dynamically updated through incremental learning, making it well-suited for online structural anomaly detection during long-term monitoring.

3 Dirichlet process-variational autoencoder-integrated incremental learning for clustering

In this section, DPVIL, a probabilistic clustering model that combines DPMM and VAE, will be described in detail. In this work, this framework takes high-dimensional TF vectors as input, extracting low-dimensional latent representations through a probabilistic encoder while identifying distinct patterns from them by introducing a DPMM into the latent space. Simultaneously, a probabilistic decoder is used to reconstruct the inputs based on latent representations drawn from the mixture distribution modeled by the DPMM. Similar to vanilla VAEs [43], the decoder, conditioned on a DPMM prior, models the generative process of raw TF vectors, while the encoder, along with another DPMM, approximates the true posterior over the generative model’s parameters through variational inference. This design enables the DPMM to regularize the latent space of the VAE, allowing DPVIL to extract discriminative representations for clustering. For structural anomaly detection, each

cluster identified in the latent space of DPVIL represents a distinct pattern of structural behavior. Healthy states can be determined using labels of normal condition data provided a priori, while other clusters denote different damage patterns. Fig. 3 presents a schematic illustration of DPVIL, with the symbols defined in Section 2.

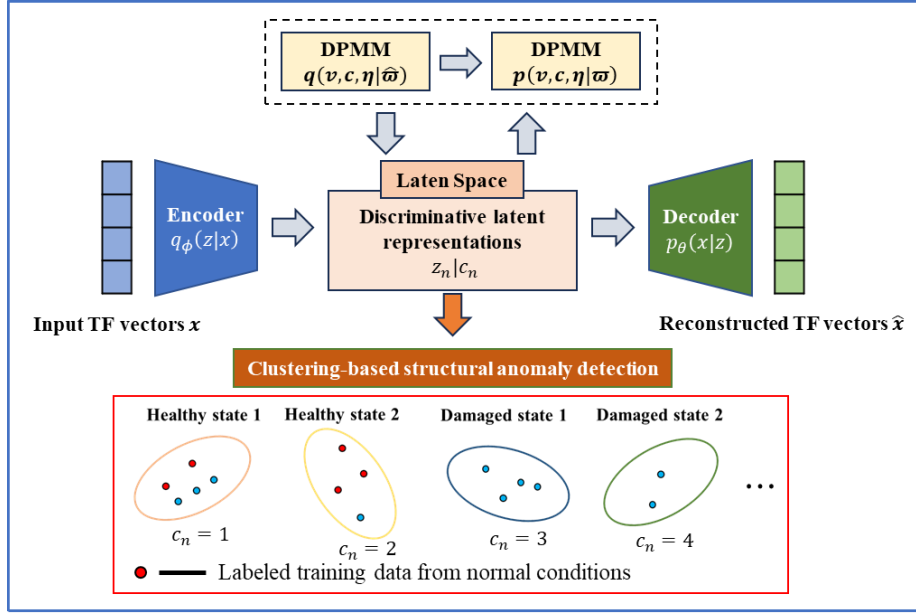


Figure 3. Schematic diagram of DPVIL for clustering in structural anomaly detection.

3.1 The generative process

Since DPVIL is an unsupervised generative approach to clustering, the random process through which raw TF vectors are generated is introduced first. Specifically, an observed sample $x_n \in \mathcal{R}^D$ is generated by the following process within the context of DPVIL, with a schematic diagram provided in Fig. 4 to facilitate illustration.

Generative process of DPVIL:

1. Draw a sample $v_k \sim \text{Beta}(1, \alpha)$
 2. Draw an assignment variable $c_n \sim \text{Cat}(\pi_k(v))$, $\pi_k(v) = v_k \prod_{i=1}^{k-1} (1 - v_i)$, where
-

$\text{Cat}(\bullet)$ is the categorical distribution

3. Draw a sample of component parameters $\eta \sim H(\eta|\varphi)$
 4. Draw a latent variable $z_n|c_n \sim F(z|\eta_{c_n})$
 5. Draw a sample x_n (here we assume x_n is real-valued):
 - 1) Compute the mean and standard deviation $[\mu_x, \sigma_x] = f(z, \theta)$,
where $f(\bullet)$ is a function modeled by a neural network
 - 2) Draw a sample $x_n \sim \mathcal{N}(\mu_x, \sigma_x^2 I)$
-

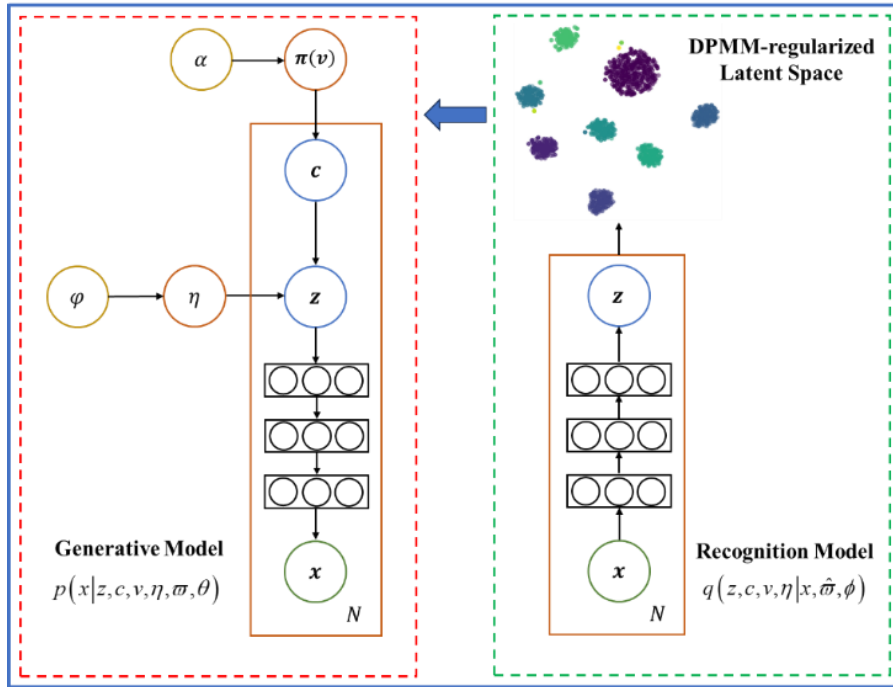


Figure 4. Schematic illustration of generative process of DPVILL.

Based on this generative model, the goal is to optimize the parameters to mimic the underlying random process through which the TF vectors are generated. To achieve this, a recognition model $q(z, c, v, \eta|x, \hat{\omega}, \phi)$ is introduced to approximate the true posterior $p(z, c, v, \eta|x, \omega, \theta)$, following the approach in [43]. This method incorporates a DPMM prior into the latent space of vanilla VAEs, thus providing DPVILL with both generative

modeling and clustering capabilities. For the detailed analysis, the true posterior distribution representing the generative process of DPVILL can be expressed as:

$$\begin{aligned}
p(z, c, v, \eta, \theta | \varpi, x) &= \frac{p(z, c, v, \eta | \varpi) p(x | z, \theta)}{\log p(x | \varpi, \theta)} \\
&\propto p(c, v, \eta | \varpi) p(z | c, \eta) p(x | z, \theta) \\
&= p(v | \alpha) p(c | v) p(\eta | \varphi) p(z | c, \eta) p(x | z, \theta)
\end{aligned} \tag{5}$$

Here $F(\cdot)$ is assumed to be Gaussian and $H(\cdot)$ is set as the corresponding conjugate prior, then it has:

$$\begin{aligned}
p(v | \alpha) &= \text{Beta}(1, \alpha) \\
p(c | v) &= \text{Cat}(\pi_k(v)) \\
H(\eta | \varphi) &= p(\mu, \Lambda | \varphi) = \mathcal{NW}(\mu, \Lambda | m, \lambda, \mathbf{W}, \nu) \\
F(z | \eta_c) &= p(z | c, \eta) = \mathcal{N}(z | \mu_c, (\Lambda_c)^{-1}) \\
p(x | z, \theta) &= \mathcal{N}(\mu_x, \sigma_x^2 I); [\mu_x, \sigma_x] = f(z, \theta)
\end{aligned}$$

where $\mathcal{NW}(\cdot)$ is the normal-Wishart distribution; μ and Λ denote the mean vector and precision matrix of the Gaussian distribution, respectively.

3.2 Variational inference for DPVILL

3.2.1 Tighter lower bound on log marginal likelihood of DPVILL

As the true posterior is typically intractable, a variational distribution (the recognition model) is introduced to approximate the true posterior by minimizing the KL divergence between them, which can be expressed as:

$$\begin{aligned}
&D_{KL} \left(q(z, c, v, \eta | x, \hat{w}, \phi) \parallel p(z, c, v, \eta, \theta | \varpi, x) \right) \\
&= \log p(x | \varpi, \theta) - \mathbb{E}_{q(z, c, v, \eta | x, \hat{w}, \phi)} \left[\log \frac{p(x, z, c, v, \eta, \theta | \varpi)}{q(z, c, v, \eta | x, \hat{w}, \phi)} \right] \\
&\triangleq \log p(x | \varpi, \theta) - \mathcal{L}_{ELBO}(\theta, \phi, \hat{w} | x)
\end{aligned} \tag{6}$$

Therefore, minimizing the KL divergence is equivalent to maximizing the evidence lower bound (ELBO) $\mathcal{L}_{ELBO}(\theta, \phi, \hat{\omega}|x)$ through optimizing the parameters $\theta, \phi, \hat{\omega}$, which can be rewritten as:

$$\mathcal{L}_{ELBO}(\theta, \phi, \hat{\omega}|x) = \mathbb{E}_{q(z|x, \phi)} [\log p(x|z, \theta)] - D_{KL} [q(z, c, v, \eta|x, \hat{\omega}, \phi) \| p(z, c, v, \eta|\varpi)] \quad (7)$$

To facilitate the optimization process, a fully factorized variational distribution is adopted here based on the mean field assumption, while the variational distribution of the DPMM is chosen to belong to the same family as the true posterior distribution [20].

As a result, the variational distribution can be expressed as:

$$q(z, c, v, \eta|x, \hat{\omega}, \phi) = q(z|x, \phi)q(c, v, \eta|z, \hat{\omega}) = q(z|x, \phi)q(v|z, \hat{\alpha})q(c|z, \hat{\pi})q(\eta|z, \hat{\phi}) \quad (8)$$

where each factor can be expressed as $q(v|z, \hat{\alpha}) = \text{Beta}(\hat{\alpha}_1, \hat{\alpha}_2)$, $q(c|z, \hat{\pi}) = \text{Cat}(\hat{\pi}_k)$, and $q(\eta|z, \hat{\phi}) = q(\mu, \Lambda|z, \hat{\phi}) = \mathcal{NW}(\mu, \Lambda|\hat{m}, \hat{\lambda}, \hat{W}, \hat{v})$. Additionally, similar to vanilla VAEs [43], $q(z|x, \phi)$ is modeled using a Gaussian neural network g :

$$[\mu_z, \sigma_z] = g(x, \phi); z \sim \mathcal{N}(\mu_z, \sigma_z^2 I)$$

For a single data point x_n , the first term in Eq. (7), $\mathbb{E}_{q(z_n|x_n, \phi)} [\log p(x_n|z_n, \theta)]$, also referred to as the reconstruction loss, can be estimated using the stochastic gradient variational Bayes (SGVB) estimator and the reparameterization trick [43]:

$$\mathbb{E}_{q(z_n|x_n, \phi)} [\log p(x_n|z_n, \theta)] \approx \frac{1}{L} \sum_{l=1}^L \log p(x_n|z_n^{(l)}, \theta) \quad (9)$$

where $z_n^{(l)}$ is a sample drawn from the variational posterior distribution, i.e.,

$z_n^{(l)} \sim q(z_n|x_n, \phi)$, and is given by [43]:

$$z_n^{(l)} = g_\phi(\epsilon_n^{(l)}, x_n) = \mu_{z_n} + \sigma_{z_n} \odot \epsilon_n^{(l)}; \epsilon_n^{(l)} \sim \mathcal{N}(0, I) \quad (10)$$

Based on this approach, the reconstruction loss can be estimated, while the KL

divergence term $D_{KL} [q(z, c, v, \eta | x, \hat{\omega}, \phi) \| p(z, c, v, \eta | \varpi)]$ is analytically intractable as it involves a complex partition of the latent space through a DPMM. To address this, a lower bound on the log marginal likelihood of DPVILL is derived as the objective function for jointly optimizing the DPMM and network parameters, which is tighter than the ELBO given sufficient training data and an appropriate penalizing hyperparameter γ , and is expressed as follows:

$$\begin{aligned} \mathcal{L}(\theta, \phi, \hat{\omega} | x) = & \mathbb{E}_{q(z|x, \phi)} [\log p(x|z, \theta)] + \mathbb{E}_{q(c, v, \eta | \hat{\omega})} \left[\log \frac{p(c, v, \eta | \varpi)}{q(c, v, \eta | z, \hat{\omega})} \right] \\ & - \gamma \sum_{k=1}^{\infty} q(c=k) D_{KL} \left[q(z|x, \phi) \left\| \mathcal{N} \left(z \mid \hat{m}_k, (\hat{\lambda}_k \hat{W}_k)^{-1} \right) \right. \right] \end{aligned} \quad (11)$$

where $\hat{\omega} = \{\hat{m}, \hat{\lambda}, \hat{W}, \hat{v}\} = \{\hat{m}_k, \hat{\lambda}_k, \hat{W}_k, \hat{v}_k\}_{k=1}^{\infty}$ denotes the parameters of the variational distribution $q(\eta | z, \hat{\omega}) = \mathcal{NW}(\mu, \Lambda | \hat{m}, \hat{\lambda}, \hat{W}, \hat{v})$. The detailed derivation of this tighter lower bound is provided in [Appendix I](#).

3.2.2 Two-step iterative optimization approach for inferring DPVILL

Although this lower bound is tractable, optimizing θ , ϕ , and $\hat{\omega}$ simultaneously remains challenging as the DPMM involves countably infinite number of components [40]. To address this issue, a two-step approach is proposed to iteratively optimize the DPMM parameters $\hat{\omega}$ and the network parameters θ, ϕ given the training set $X = \{x_n\}_{n=1}^N$. In each iteration, this approach firstly updates $\hat{\omega}$ through CAVI using extracted latent representations, while automatically inferring the number of active components. Subsequently, θ and ϕ are updated using SGVB with the objective function given in Eq. (11), keeping the DPMM parameters fixed and omitting the inactive components. This iterative process can be summarized as follows:

- (1) Fix the network parameters θ and ϕ , and optimize the DPMM parameters $\hat{\omega}$

using a CAVI optimizer with a greedy split-merge scheme based on the set of reparameterized latent variables $Z = \{z_n\}_{n=1}^N$, which will be described in detail in the next section. In this step, the objective becomes maximizing an ELBO with respect to $\hat{\omega}$, denoted by $\mathcal{L}_{CAVI}(\hat{\omega}|Z) = \mathbb{E}_{q(c,v,\eta|\hat{\omega})} \left[\log \frac{p(Z,c,v,\eta|\varpi)}{q(c,v,\eta|Z,\hat{\omega})} \right]$. The CAVI method determines the number of active components K_a based on the latent representations extracted by the encoder, as well as the optimized variational parameters of the DPMM, i.e., $\hat{\omega} = \{\hat{\alpha}_k, \hat{\phi}_k, \hat{\pi}_{nk}\}_{k=1,2,\dots,K_a}^{n=1,2,\dots,N}$, which allows for calculating $\mathcal{L}(\theta, \phi, \hat{\omega}|x)$ by omitting the inactive components when optimizing the network parameters.

- (2) Fix the DPMM parameters K_a and $\hat{\omega}$, and optimize the network parameters θ and ϕ using the SGVB estimator and the reparameterization trick [43]. In this scenario, the term $\mathbb{E}_{q(c,v,\eta|z,\hat{\omega})} \left[\log \frac{q(c,v,\eta|z_n,\hat{\omega})}{p(c,v,\eta|\varpi)} \right]$ can be ignored as it is irrelevant to θ and ϕ , and the objective function becomes:

$$\begin{aligned} \mathcal{L}(\theta, \phi, \hat{\omega}|X) &= \mathcal{L}(\theta, \phi|\hat{\omega}, X) = \sum_{n=1}^N \mathcal{L}(\theta, \phi|\hat{\omega}, x_n) \\ &= \sum_{n=1}^N \mathbb{E}_{q(z_n|x_n,\phi)} \left[\log p(x_n|z_n,\theta) \right] - \gamma \sum_{k=1}^{K_a} q(c=k) \mathcal{D}_{KL} \left[q(z_n|x_n,\phi) \parallel \mathcal{N} \left(z_n \mid \hat{m}_k, (\hat{\lambda}_k \hat{W}_k)^{-1} \right) \right] \end{aligned} \quad (12)$$

where $\mathbb{E}_{q(z_n|x_n,\phi)} \left[\log p(x_n|z_n,\theta) \right]$ is given in Eq. (9). Given a minibatch of data

$X_B = \{x_n\}_{n=1}^B$ randomly drawn from the training set, the objective function can be

$$\text{approximated by } \mathcal{L}(\theta, \phi|\hat{\omega}, X) \simeq \mathcal{L}^B(\theta, \phi|\hat{\omega}, X^B) = \frac{N}{B} \sum_{n=1}^B \mathcal{L}(\theta, \phi|\hat{\omega}, x_n) \quad [43].$$

By conducting these two steps in each training epoch, the DPMM parameters $\hat{\omega}$, the number of active components K_a , and the network parameters θ and ϕ , can be

iteratively updated until convergence, allowing DPVILL to model the generative process of raw data while simultaneously extracting discriminative features for clustering.

3.3 Greedy split-merge scheme-based CAVI for the DPMM

Given the latent representations extracted from the training set, a CAVI optimizer is developed to obtain K_a and $\hat{\omega}$, which is a modified version of the method proposed in [20]. As a result, only a schematic overview of the optimization procedures is provided here. For detailed derivations of the update equations for each parameter, one can refer to [20]. Since the CAVI optimizer is integrated into the optimization pipeline of DPVILL, each training sample is processed once in each training epoch, making it unsuitable to retain information about previous data by directly using the previous variational posterior as the new prior, as employed in [20]. To address this issue, the CAVI optimizer in this work leverages the summary statistics [39] to cache the information of previous data, as the posterior can be derived from the prior and the summary statistics [20]. Specifically, as the components of the DPMM are Gaussian distributions here, the summary statistics can be expressed as follows when omitting the inactive components:

$$s(Z) = \{s_k(Z)\}_{k=1}^{K_a} = \{N_k, \bar{z}_k, S_k\}_{k=1}^{K_a} \quad (13)$$

where $N_k = \sum_{n=1}^N \hat{\pi}_{nk}$, $\bar{z}_k = \frac{1}{N_k} \sum_{n=1}^N \hat{\pi}_{nk} z_n$, $S_k = \frac{1}{N_k} \sum_{n=1}^N \hat{\pi}_{nk} (z_n - \bar{z}_k)(z_n - \bar{z}_k)^T$. Conditioned on

the summary statistics, the CAVI optimizer involves the following two steps:

(1) **Greedy split:** This step starts from $K_a = 1$ and iteratively splits the component

that maximally increases the ELBO $\mathcal{L}_{CAVI}(\hat{\omega}|Z)$, which accelerates convergence compared to the method proposed in [20] due to its greedy nature. Specifically, in each iteration, a component k is split into two components k_1 and k_2 along the bisector of its principal component, as suggested in [42]. Subsequently, the summary statistics for these two components $s_{k_1}(Z)$ and $s_{k_2}(Z)$ are updated using the coordinate ascent algorithm, while the summary statistics for the other components remain fixed. Then, the ELBO is calculated and cached. This process is repeated for all active components to identify the split that maximizes the ELBO. Afterward, the selected component is split, and the summary statistics for all components are updated to compute a new ELBO after the split, denoted by $\mathcal{L}_{CAVI}^S(\hat{\omega}|Z)$. If $\mathcal{L}_{CAVI}^S(\hat{\omega}|Z) > \mathcal{L}_{CAVI}(\hat{\omega}|Z)$, the split is accepted with the number of active components updated to $K_a = K_a + 1$, and another iteration of splitting is initiated. Otherwise, the split is rejected, and the greedy split step is terminated. This step iteratively splits active components through a greed search to determine the optimal parameters K_a and $\hat{\omega}$. However, due to its greedy nature, the split step tends to be affected by outliers and generate isolated components, leading to increased computational costs as training progresses [39]. To mitigate this issue, a greedy merge step is introduced to avoid local optima and reduce redundant isolated components.

- (2) **Greedy merge:** This step seeks to maximize the ELBO by iteratively merging two active components k_1 and k_2 using a greedy search. As randomly select k_1 and k_2 to merge is computationally expensive and unlikely to yield an improved the

ELBO, the method proposed in [39] is employed as a pre-selecting approach. Specifically, after selecting k_1 at random, k_2 is chosen based on a criterion that maximizes the ratio of marginal likelihoods between the merged and separate configurations. Assume the merged component is denoted by k_{12} , the summary statistics of this merged component is $s_{k_{12}}(Z) = s_{k_1}(Z) + s_{k_2}(Z)$ [39], and the ratio of marginal likelihoods is given by:

$$p(k_2|k_1) \propto \frac{M(s_{k_{12}}(Z))}{M(s_{k_1}(Z))M(s_{k_2}(Z))} \quad (14)$$

This ratio can be easily computed with cached summary statistics and is given in [39], while the ELBO after merging can be derived based on $s_{k_{12}}(Z)$ [20]. In each iteration, the pair of components merging which maximizing the ELBO is merged, and the corresponding ELBO, denoted by $\mathcal{L}_{CAVI}^M(\hat{\omega}|Z)$, is computed. If $\mathcal{L}_{CAVI}^M(\hat{\omega}|Z) > \mathcal{L}_{CAVI}(\hat{\omega}|Z)$, the merged configuration is accepted, and the next merge iteration is performed. Otherwise, the merge is rejected, and the greedy merge step is stopped.

Based on these two steps, the number of active components K_a and the optimized variational parameters of the DPMM $\hat{\omega} = \{\hat{\alpha}_k, \hat{\varphi}_k, \hat{\pi}_{nk}\}_{k=1,2,\dots,K_a}^{n=1,2,\dots,N}$ can be derived through a greedy split-merge scheme given the latent variables Z . To provide an intuitive illustration, the optimization process is summarized in [Algorithm 1](#):

Algorithm 1: Greedy split-merge scheme-based CAVI for the DPMM

Require: latent variables $Z = \{z_n\}_{n=1}^N$.

Initialize: $K_a = 1$; prior parameters $\varpi = \{\alpha, \varphi\}$; initial summary statistics $s_k(Z)$ and lower bound $\mathcal{L}_{CAVI}(\hat{\omega}|Z)$.

A. Greedy split step:**Repeat:**

(A1) For each component $k \leq K_a$, do:

- Split component k into two components k_1 and k_2 .
- Update the summary statistics $s_{k_1}(Z)$ and $s_{k_2}(Z)$, with the summary statistics for the other components fixed.
- Calculate the new ELBO $\mathcal{L}_{CAVI}^{S_k}(\hat{\omega}|Z)$ and revert to the configuration before splitting.

(A2) Identify the component K with $\mathcal{L}_{CAVI}^{S_K}(\hat{\omega}|Z) = \max\{\mathcal{L}_{CAVI}^{S_k}(\hat{\omega}|Z)\}_{k=1}^{K_a}$ and split it into two components.

(A3) Update $s_k(Z)$ for all $k \leq K_a + 1$ and compute the ELBO after splitting, denoted by $\mathcal{L}_{CAVI}^S(\hat{\omega}|Z)$.

(A4) If $\frac{\mathcal{L}_{CAVI}^S(\hat{\omega}|Z) - \mathcal{L}_{CAVI}(\hat{\omega}|Z)}{\mathcal{L}_{CAVI}(\hat{\omega}|Z)} > \tau$, set $K_a = K_a + 1$, $\mathcal{L}_{CAVI}(\hat{\omega}|Z) = \mathcal{L}_{CAVI}^S(\hat{\omega}|Z)$,

and go to step (A1), else break the loop.

B. Greedy merge step:**Repeat:**

(B1) For each component $k \leq K_a$, do:

- Compute $p(k_2|k_1)$ according to Eq. (14) for all $k_2 \leq K_a$ and $k_2 \neq k_1$.
- Merge the pair (k_1, k_2) with the maximum $p(k_2|k_1)$ into one component k_{12} .
- Compute the summary statistics $s_{k_{12}}(Z)$ and the new ELBO after merging $\mathcal{L}_{CAVI}^{M(k_1, k_2)}(\hat{\omega}|Z)$, then revert to the configuration before merging.

(B2) Find the pair (K_1, K_2) with $\mathcal{L}_{CAVI}^{M(K_1, K_2)}(\hat{\omega}|Z) = \max\{\mathcal{L}_{CAVI}^{M(k_1, k_2)}(\hat{\omega}|Z)\}_{k_1=1}^{K_a}$ and merge them into one component K_{12} .

(B3) Update the summary statistics for all components and compute the ELBO after merging, denoted by $\mathcal{L}_{CAVI}^M(\hat{\omega}|Z)$.

$$(B4) \text{ If } \frac{\mathcal{L}_{CAVI}^M(\hat{w}|Z) - \mathcal{L}_{CAVI}(\hat{w}|Z)}{\mathcal{L}_{CAVI}(\hat{w}|Z)} > \tau, \text{ set } K_a = K_a - 1, \mathcal{L}_{CAVI}(\hat{w}|Z) = \mathcal{L}_{CAVI}^M(\hat{w}|Z),$$

and go to step (B1), else break the loop.

Compute the variational posterior based on the prior and the summary statistics.

Output: Number of active components K_a ; summary statistics $\{s_k(Z)\}_{k=1}^{K_a}$;

optimized variational parameters $\hat{w} = \{\hat{\alpha}_k, \hat{\phi}_k, \hat{\pi}_{nk}\}_{k=1,2,\dots,K_a}^{n=1,2,\dots,N}$.

3.4 Training procedure of DPVILL

Based on Section 3.2 and Section 3.3, the detailed procedures of optimizing

DPVILL can be summarized as follows:

Algorithm 2: DPVILL

Input: Dataset $X = \{x_n\}_{n=1}^N$, batch size B , initial network parameters θ and ϕ , initial parameters of the DPMM $K_a = 1$, $\varpi = \{\alpha, \phi\}$, $s_k(Z)$.

Output: Optimized network parameters θ, ϕ and DPMM parameters

$$K_a, \hat{w} = \{\hat{\alpha}_k, \hat{\phi}_k, \hat{\pi}_{nk}\}_{k=1,2,\dots,K_a}^{n=1,2,\dots,N}, \{s_k(Z)\}_{k=1}^{K_a}.$$

1. Repeat:

2. Create an empty dataset $Z = \emptyset$ to store the latent representations of each minibatch.
 3. For each minibatch, do:
 4. Sample a batch of data $X^B = \{x_n\}_{n=1}^B$ from the dataset X .
 5. Fix the DPMM parameters, compute the objective function for the neural networks $\mathcal{L}^B(\theta, \phi | \hat{w}, X^B)$.
 6. Compute the gradients of minibatch estimator $\nabla_{\theta, \phi} \mathcal{L}^B(\theta, \phi | \hat{w}, X^B)$.
 7. Update the parameters θ, ϕ using the gradients.
 8. Obtain the latent representations of current minibatch $Z^B = \{z_n\}_{n=1}^B$ through the reparameterization trick and store them into the dataset $Z = Z \cup Z^B$.
 9. Fix the network parameters θ, ϕ and update the parameters of the DPMM
-

$K_a, \hat{\omega} = \{\hat{\alpha}_k, \hat{\phi}_k, \hat{\pi}_{nk}\}_{k=1,2,\dots,K_a}^{n=1,2,\dots,N}, \{s_k(Z)\}_{k=1}^{K_a}$ using the stored latent representations

according to [Algorithm 1](#).

10. Reset the dataset $Z = \emptyset$.

11. **Until Convergence.**

[Algorithm 2](#) enables jointly optimizing the network and DPMM parameters through an iterative approach, resulting in an optimized DPVIL capable of extracting discriminative representations from raw data for both clustering and data generation. Notably, as the entire optimization process alternates between updating the DPMM and the VAE, less rigorous convergence criteria can be used to improve the training efficiency of DPVIL. For incremental learning, information from previous data can be effectively retained through the summary statistics of the DPMM and the network parameters, allowing DPVIL to dynamically adapt to new data in a few-shot or even zero-shot manner [39]. This capability is crucial for real-world SHM problems, where different patterns of dynamic responses are gradually observed as the shift of structural conditions during the operating process [20, 21]. This requires the SHM system to efficiently recognize and learn new patterns from incoming data without forgetting previously acquired knowledge, highlighting the significance of incremental learning in this context. Additionally, different from directly using the DPMM to cluster the latent space of a vanilla VAE, where the DPMM and VAE are optimized separately, the joint optimization scheme regularizes the latent representations to align with a DPMM manifold [32], promoting DPVIL to extract discriminative features, dynamically adapt the number and shape of clusters, and effectively capture the underlying structure of the data during optimization. The differences between these two approaches will be

discussed in detail in the case studies. Furthermore, while DPVIIL is used as an illustrative example in this work, the proposed framework can be flexibly generalized to some other DGMs. For example, DPGIIL can be applied to flow-based DGMs [31] by introducing a normalizing flow in the latent space to transform the original latent representation z into a variable z_K with a more complex distribution, while the objective function given in Eq. (11) can then be modified accordingly using the method described in [31]. This approach provides a more flexible latent space for representation learning but incurs higher computational costs.

4 Procedures of TF-based online structural anomaly detection with DPVIIL

For TF-based online structural anomaly detection, DPVIIL leverages its capabilities of representation learning and incremental clustering to extract latent representations from high-dimensional raw TF vectors and cluster them to indicate different patterns of structural behavior. This approach capitalizes on the sensitivity of TFs to structural damage and their robustness to excitation. It also incorporates comprehensive frequency domain information by utilizing TF vectors over a wide frequency band while avoiding the need for dimensionality reduction through manual feature selection. In practice, a set of TF vectors from normal operating conditions is initially used to identify the clusters denoting the healthy states. In the subsequent monitoring phase, as new TF vectors gradually flow into the system, the DPVIIL is incrementally updated to adapt to observed data. The structural condition is determined based on the clustering results: If the latent representation of a TF vector is assigned to one of the clusters representing the normal operating conditions, the structure is

considered healthy; otherwise, it indicates the existence of structural damage. The detailed procedures are illustrated in Fig. 5. Apart from structural anomaly detection, this method can be flexibly applied to semi-supervised tasks to provide more insights into different structural conditions if the identified clusters can be labeled during operation and incorporated into future analysis [21], which requires much less labeled training data compared to traditional supervised methods. For a detailed discussion on applying clustering methods in semi-supervised SHM, one can refer to [21].

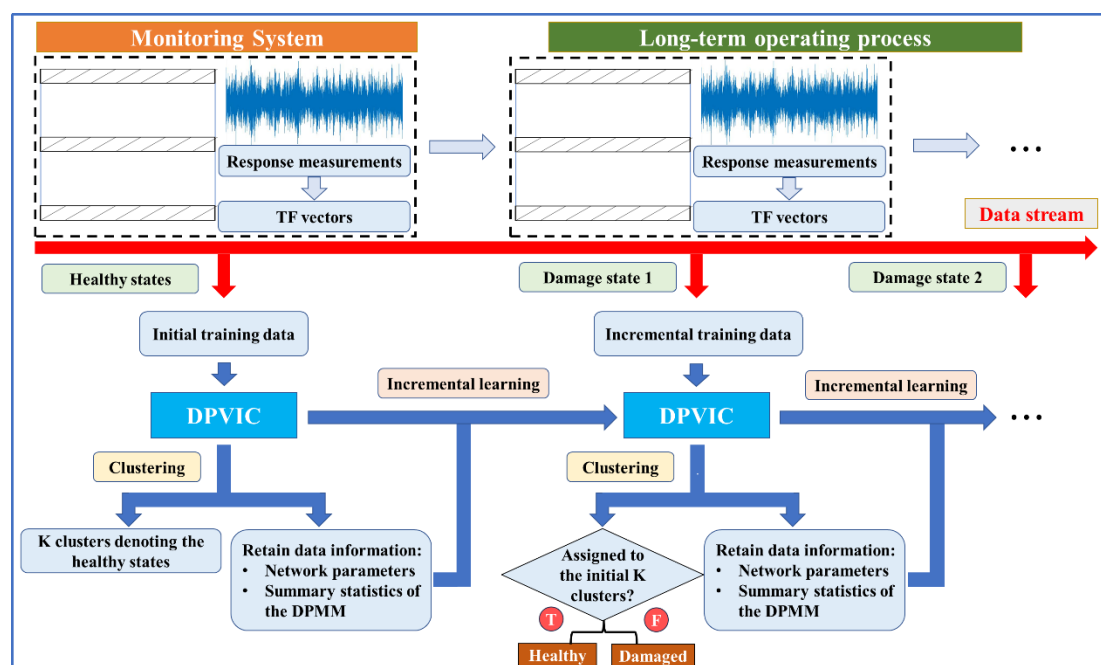


Figure 5. Procedures of DPVIL for clustering in TF-based online structural anomaly detection.

5 Case Studies

5.1 Structure description

The performance of the proposed framework will be validated through two case studies, including an 8-story numerical shear building and a benchmark dataset obtained from the S101 bridge. In both case studies, the input to DPVIL consists of

vectors containing the magnitudes of TFs derived from raw acceleration measurements between two adjacent sensors over a wide frequency band that encompasses multiple natural frequencies of the monitored structure. To assess the performance of DPVILL in online structural anomaly detection and clustering, four performance metrics, including the damage detection accuracy (DDA), unsupervised clustering accuracy (ACC) [35], adjusted rand index (ARI) [44], and normalized mutual information (NMI) [44], are employed, with higher values indicating better performance across all metrics. DDA evaluates the model's ability to detect structural anomalies by distinguishing between normal and damaged states using different clusters. ACC compares the unsupervised cluster assignments with the ground truth labels, and then finds the best matching between them through the Hungarian algorithm [35]. ARI and NMI assess clustering performance by measuring the differences between inferred cluster assignments and the ground truth labels [44]. Therefore, ground truth class labels are added in both case studies for performance evaluation but are not used during training.

For the numerical structure, the stiffness and mass of each floor are set as $K_i = 2.5 \times 10^6 \text{ N/m}$ and $m_i = 1000 \text{ kg}$, respectively. Classical Rayleigh damping is applied with the damping ratios for the first two modes assumed to be $\zeta_1 = \zeta_2 = 1\%$. In addition to the healthy condition, seven damage patterns are simulated by reducing the stiffness of certain floors, as summarized in [Table 1](#). The structure is excited by an ambient input at the first floor, which is modeled as Gaussian white noise with an auto-PSD of $0.5 \text{ m}^2 \text{ s}^{-3}$. The obtained responses are contaminated by Gaussian white noise with a signal to noise ratio of 20dB to simulate the effect of measurement error. The

sampling duration is set as 300s with a sampling frequency of 50Hz. A total of 2000 acceleration samples are generated to construct TF vectors, with the first 600 from the healthy condition and the remaining 1400 from different damage scenarios. This imbalance is designed to simulate real-world SHM scenarios.

Table 1. Damage scenarios for the 8-story numerical shear building.

Scenario	Damaged floor	Damage extent	No. of samples	Class label
Healthy state	-	-	600	0
Damage scenario 1	1	5%	200	1
Damage scenario 2	1	10%	200	2
Damage scenario 3	2 4	10% 10%	200	3
Damage scenario 4	1 3 5	10% 15% 20%	200	4
Damage scenario 5	2 4 6	15% 20% 25%	200	5
Damage scenario 6	1 3 5 7	10% 15% 20% 25%	200	6
Damage scenario 7	1 2 4 6 8	10% 15% 20% 25% 30%	200	7

The S101 bridge dataset contains response measurements from a progressive damage test conducted on the bridge [45]. The sampling frequency of the sensors was set as 500Hz with each measurement lasting 5.5 minutes. These raw measurements were further divided into shorter segments with each lasting 150s to construct TF vectors, resulting in a dataset with the size of 75000×662 for each sensor. The damage

test artificially introduced two major damage scenarios [45]. In the first, the northwestern pier of the bridge was lowered stepwise by about 3cm, and in the second, several tendons were cut to simulate the effects of local prestressing reinforcement loss. Between these two damage scenarios, repair work was carried out to simulate real-world bridge maintenance. Four class labels are manually assigned to the dataset as ground truth to evaluate the clustering performance of DPVIL, aiming to verify its capability to distinguish between different damage scenarios in real-world bridge structures. The damage actions and their corresponding labels are summarized in [Table 2](#). It is worth mentioning that the original state A (begin of cutting through column) in [45] is excluded here, as it represents a transition from a healthy state to a damaged condition [45], which cannot be adequately described by a single class label. For more details on the S101 bridge and the progressive damage test, one can refer to [45].

Table 2. Notation of consecutive damage actions acted on the S101 bridge and their corresponding labels.

State No.	Damage action	Damage effect	Class label
A	No action	♦ Baseline	0
B	End of second cut through the pier	♦ Formation of an extra hinge just above the foundation, which itself is equivalent to a constructive fixed support	
C	1st step of the pier settlement (10mm)	♦ Moderate noise	1
D	2nd step of the pier settlement (20 mm)	♦ Horizontal cracks are found in neighboring pier	
E	3rd step of the pier settlement (27 mm)	♦ Settling of bridge deck until reaching the elastic limits, support is not lost	

			completely due to the hydraulic jack	
F	Inserting steel plates	♦		
G	Uplifting the damaged pier	♦	Some occurred cracks are closed	2
		♦	The hinge caused by cutting remains	
H	Exposing cables and cutting of 1st cable	♦	Reduction of prestressing without indication of the change of conditions	
I	Cutting through 2nd cable	♦	No obvious influence on structural behavior since bridge is not loaded by traffic	3
J	Cutting through 3rd cable	♦		
K	Partly cutting of 4th cable	♦	The extra prestressing reservoir is run out	

In both case studies, the same model architecture of DPVIL is used, as detailed in [Appendix II](#). Each experiment is repeated five times, with the model trained to converge in each run. The average performance and standard deviation are recorded for analysis.

5.2 Online structural anomaly detection based on incremental learning

For online structural anomaly detection, DPVIL is initially trained on a dataset containing only TF vectors from the normal condition. Subsequently, TF vectors from different damage scenarios are gradually observed and incorporated into the training process, which is a class-incremental problem in the context of incremental learning [46] and aligns with real-world structural anomaly detection scenarios. The ACC of DPVIL across training epochs for both case studies is presented in [Fig. 6](#). In the numerical case study, DPVIL is initially trained on data from class 0 (the healthy state), with the number of classes (structural conditions) increased to 3, 5, and 8 at epochs 40, 80, and 190, respectively. For the S101 bridge case study, the model is first trained on

data from class 0, and data from the remaining three structural states are incorporated at epochs 60, 120, and 180, respectively. As shown in Fig. 6, the dynamic adaptive capability of the proposed method is clearly demonstrated. The ACC experiences sudden decreases at the training epochs when data from new structural conditions are introduced, while it quickly recovers to high levels as the training progresses, as the information learned previously is effectively retained in the summary statistics of the DPMM and the network parameters. It is worth mentioning that the fluctuations in ACC observed during the incremental learning process can be attributed to the use of a relaxed convergence criterion in each training epoch, as described in Section 3.4.

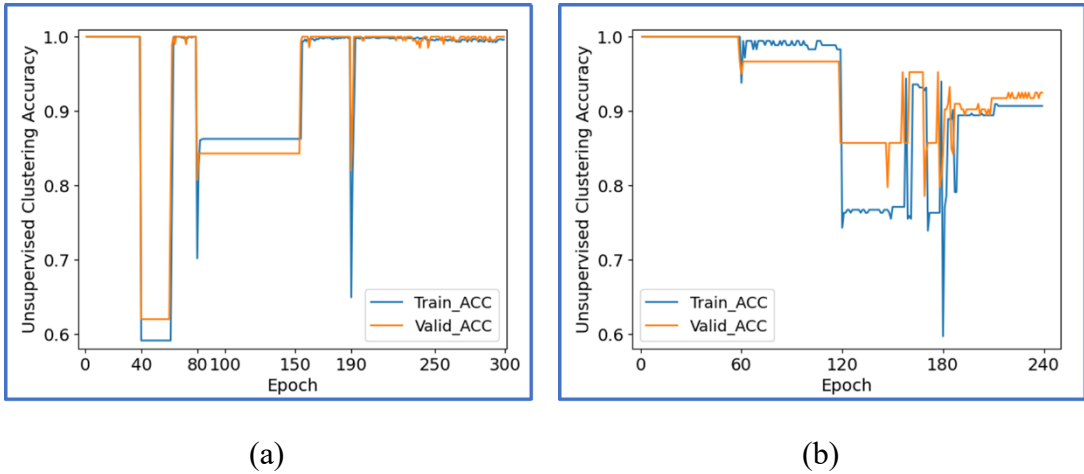
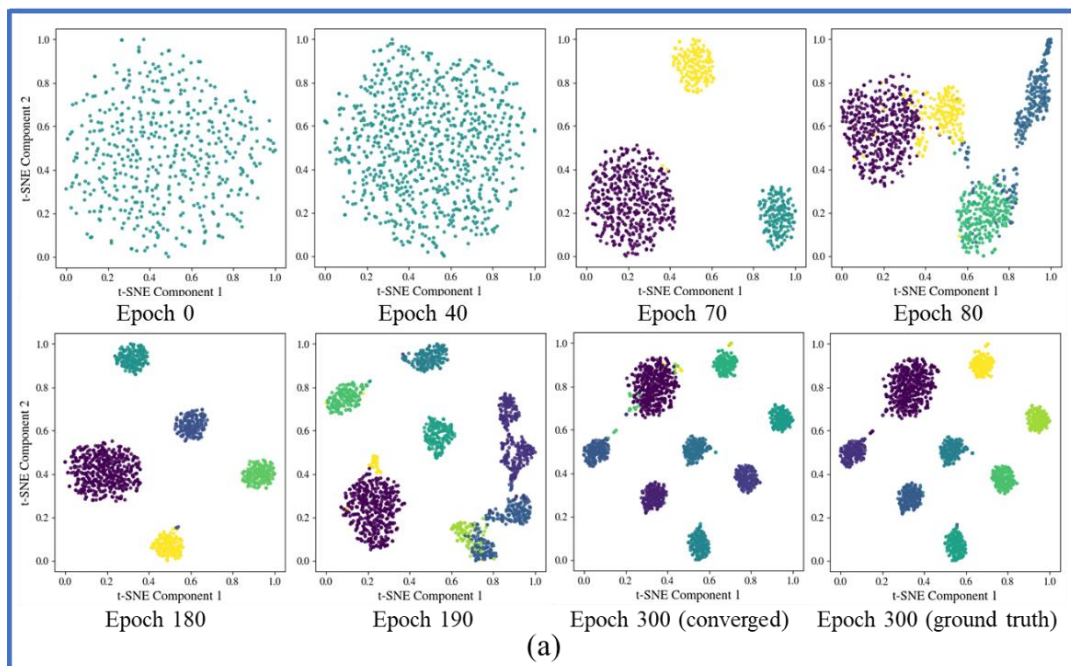


Figure 6. The variation of ACC of DPVIIL across training epochs for (a) the numerical dataset and (b) the S101 bridge dataset.

To provide a more comprehensive evaluation of the incremental learning capability of DPVIIL, t-SNE [47] plots of the latent space of DPVIIL during training are presented in Fig. 7, while the four performance metrics after observing all structural conditions are summarized in Table 3. From Fig. 7, one can find that compared to the ground truth labels, DPVIIL tends to assign samples that deviate from the center of a

class to individual clusters with small sizes. This is reasonable as DPVIL operates in a completely unsupervised manner here. For the numerical case study, all performance metrics exceed 0.95, demonstrating the sensitivity of the proposed method to changes in structural conditions. For the S101 bridge case study, the DDA and ACC remain at a high level (over 0.90), while the ARI and NMI exhibit a decrease. This can be caused by the repair work solely uplifting the damaged pier without addressing the cracks, making some vibration responses similar to those obtained at the onset of tendon cutting, as shown in Fig. 7b. These results illustrate the potential of DPVIL for real-world online structural anomaly detection tasks, due to its capability to continuously learn from incoming data without forgetting previously acquired knowledge, which makes it well-suited for the long-term monitoring of engineering structures. Additionally, as DPVIL is able to extract discriminative representations from raw data in an unsupervised manner, it can serve as a pre-training step for more complex techniques such as semi-supervised learning [20].



(a)

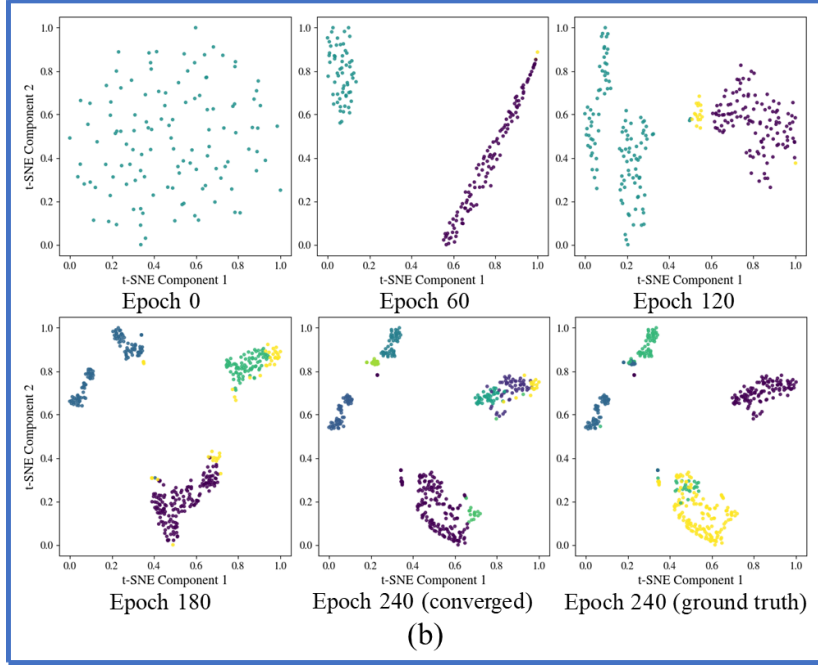


Figure 7. T-SNE plots of the latent space learned by DPVIL during training for (a) the numerical dataset and (b) the S101 bridge dataset. Different colors represent either cluster assignments or ground truth class labels.

Table 3. Performance of DPVIL in the incremental learning scenario (mean±standard deviation of 5 runs).

Dataset	Performance metrics			
	DDA	ACC	ARI	NMI
Numerical				
shear	0.9989±0.0011	0.9920±0.0045	0.9768±0.0150	0.9746±0.0157
building				
S101 bridge	0.9861±0.0065	0.9212±0.0286	0.8288±0.0553	0.8239±0.0519

5.3 Comparative studies

To further analyze the performance of DPVIL, it is compared with some state-of-

the-art clustering algorithms in these two case studies. The results of the comparative studies are presented in [Table 4](#), and the t-SNE plots of all compared approaches are shown in [Fig. 8](#). The method “DPMM+VAE” refers to using a DPMM to cluster the latent space of a vanilla VAE, with the VAE and DPMM trained separately. This approach is included to highlight the importance of the proposed joint optimization scheme in regularizing the extracted latent representations. DEC [35], which requires the number of clusters to be predefined, is tested with 6, 8, and 10 clusters on the numerical dataset and with 3, 4, and 5 clusters on the S101 bridge dataset. This setup aims to evaluate the impact of the choice of cluster number on the performance of DEC and other clustering approaches that lack the ability to dynamically adjust the cluster number. For DIVA [38], which also incorporates a DPMM, the concentration parameter is set as $\alpha = 10$ for both datasets, consistent with the configuration used for DPVILL. Additionally, as DEC is designed for clustering in static scenarios and lacks the incremental learning capability [38], the comparative studies are conducted on complete datasets including all structural conditions. The VAE architecture for all compared approaches is identical to that used in DPVILL, as detailed in [Appendix II](#), while hyperparameters are tuned according to the original papers [35, 38].

From [Table 4](#) and [Fig. 8](#), one can find that for “DPMM+VAE”, the extracted latent representations are less discriminative compared to other methods, as the objective function of the vanilla VAE fails to adequately regularize the learned latent space [32], which highlights the advantage of jointly optimizing VAE and DPMM in the proposed method. For DEC, its performance is sensitive to the choice of the number of GMM

components, with both over- and under-specification of the component number affecting its clustering performance. Additionally, the need for prespecifying the component number restricts its capability to dynamically adapt to new data for incremental learning, underscoring the advantages of employing a Bayesian nonparametric model. DIVA, on the other hand, tends to generate redundant clusters due to the relatively relaxed criterion for creating new components in the memoized online variational inference and its heuristic objective function. Compared to these approaches, DPVIIL introduces a DPMM prior into the latent space of the vanilla VAE to effectively regularize the extracted latent representations, which also endows DPVIIL with the dynamic adaptive capability for incremental learning by retaining previously learned information through summary statistics. Moreover, a reasonable optimization procedure is developed to enhance the model’s effectiveness and reliability. As a result, DPVIIL outperforms the compared methods in both structural anomaly detection and clustering performance across both case studies.

Table 4. Comparative study on complete static datasets (mean±standard deviation of 5 runs).

Dataset	Numerical shear building				S101 bridge			
Method	DDA	ACC	ARI	NMI	DDA	ACC	ARI	NMI
DPMM+V	0.9593	0.8020	0.7598	0.8814	0.9698	0.8803	0.7914	0.7805
AE	±0.0110	±0.0480	±0.0764	±0.0420	±0.0471	±0.0471	±0.0324	±0.0244
DEC-6 (3)	0.9980	0.8110	0.7832	0.9006	0.9357	0.8030	0.6623	0.6831
clusters	±0.0045	±0.0248	±0.0356	±0.0106	±0.0088	±0.0120	±0.0491	±0.0381

DEC-8 (4)	0.9990	0.9040	0.8989	0.9474	0.9543	0.8136	0.7013	0.7096
clusters	± 0.0022	± 0.0156	± 0.0194	± 0.0132	± 0.0100	± 0.0102	± 0.0211	± 0.0185
DEC-10	0.9480	0.9040	0.8046	0.9159	0.9618	0.8363	0.7594	0.7340
(5) clusters	± 0.0333	± 0.0156	± 0.0465	± 0.0121	± 0.0217	± 0.0271	± 0.0240	± 0.0363
DIVA	0.9788	0.9900	0.9251	0.9546	0.9897	0.8833	0.8060	0.7991
	± 0.0310	± 0.0117	± 0.0545	± 0.0125	± 0.0055	± 0.0463	± 0.0566	± 0.0388
DPVILL	0.9990	0.9990	0.9835	0.9876	0.9915	0.9318	0.8394	0.8349
(ours)	± 0.0022	± 0.0022	± 0.0157	± 0.0094	± 0.0031	± 0.0107	± 0.0171	± 0.0148

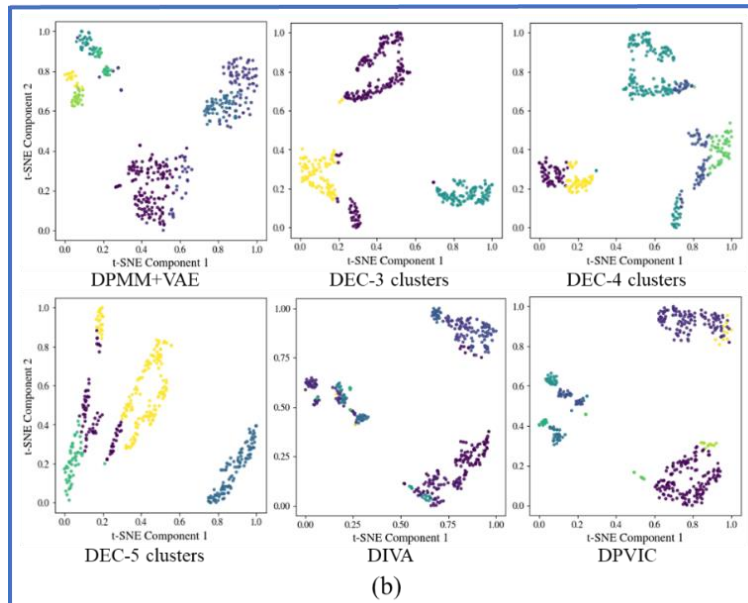
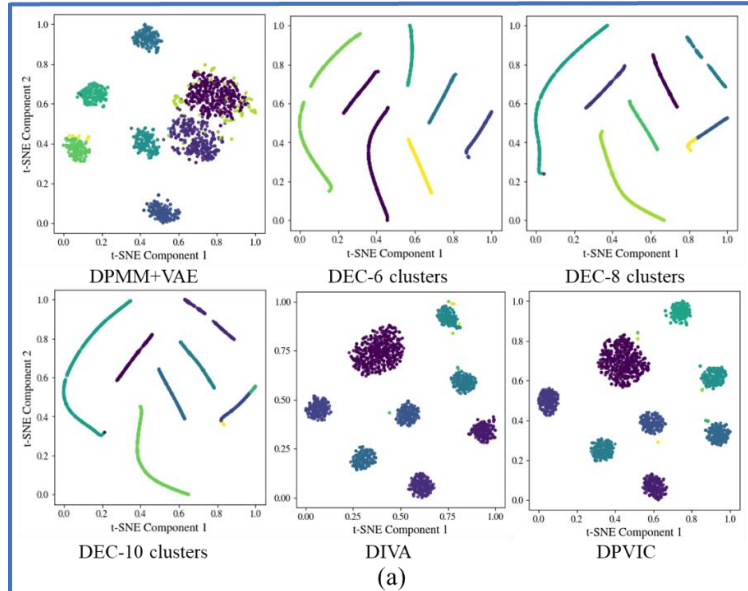


Figure 8. T-SNE plots of the latent space learned by the compared methods after convergence on (a) the numerical dataset and (b) the S101 bridge dataset. Different colors denote different cluster assignments.

5.4 Sensitivity analysis of hyperparameters

The hyperparameters of DPVIL include those related to the neural networks and the DPMM. The former can be tuned using some classical approaches [48], while the latter, especially the concentration parameter α , is more challenging to adjust, as it directly affects the number of created clusters [20]. As a result, a sensitivity analysis is conducted to investigate the stability of DPVIL with respect to α , with the results provided in Table 5. From this table, it can be found that all performance metrics exhibit only slight variations in both case studies at different levels of α . This can result from DPVIL’s iterative training process, where the DPMM regularizes the feature extraction by the neural networks, and the extracted latent representations, in turn, influence the update of DPMM parameters. As a result, the network parameters adapt automatically to different levels of α during training, leading to robust clustering performance that is less sensitive to changes in α . This sensitivity analysis illustrates the robustness of the proposed method, thereby facilitating its practical implementation.

Table 5. Sensitivity analysis of DPVIL with respect to the concentration parameter (mean±standard deviation of 5 runs).

Dataset	Numerical shear building				S101 bridge			
Alpha	DDA	ACC	ARI	NMI	DDA	ACC	ARI	NMI
0.1	0.9960 ±0.0065	0.9950 ±0.0050	0.9747 ±0.0243	0.9799 ±0.0149	0.9888 ±0.0071	0.9288 ±0.019	0.8420 ±0.0316	0.8267 ±0.0214

1	0.9900	0.9960	0.9717	0.9818	0.9891	0.9303	0.8263	0.8256
	± 0.0106	± 0.0042	± 0.0245	± 0.0128	± 0.0067	± 0.0173	± 0.0416	± 0.0317
10	0.9990	0.9990	0.9835	0.9876	0.9915	0.9318	0.8394	0.8349
	± 0.0022	± 0.0022	± 0.0157	± 0.0094	± 0.0031	± 0.0107	± 0.0171	± 0.0148
50	0.9940	0.9930	0.9758	0.9777	0.9921	0.9288	0.8352	0.8279
	± 0.0065	± 0.0084	± 0.0194	± 0.0166	± 0.0033	± 0.0115	± 0.0253	± 0.0125
100	0.9920	0.9890	0.9664	0.9698	0.9909	0.9303	0.8271	0.8246
	± 0.0076	± 0.0074	± 0.0194	± 0.0164	± 0.0028	± 0.0083	± 0.0343	± 0.0254

6 Conclusions

This work proposes DPGIIL, a novel incremental clustering framework that combines DPMM and DGM for TF-based online structural anomaly detection, while DPVIIL serves as an illustrative example. By incorporating a DPMM prior into the latent space of a vanilla VAE, DPVIIL extracts discriminative features from raw TFs for both generative modeling and clustering, while the summary statistics of the DPMM, along with the network parameters, effectively retain information about previous data to enable incremental learning. To optimize DPVIIL, a tighter lower bound on its log marginal likelihood is derived, enabling jointly optimizing the network and DPMM parameters through a two-step iterative optimization approach. Additionally, a CAVI optimizer with a greedy split-merge scheme is devised to accelerate the optimization. Two case studies demonstrate that DPVIIL outperforms some state-of-the-art methods in structural anomaly detection and clustering. This is due to the adoption of a Bayesian nonparametric model to flexibly adapt model complexity to observed data, as well as a mathematically solid optimization framework. Furthermore, the incremental learning capability allows DPVIIL to dynamically generate new clusters as new data arrive to indicate the emergence of new structural conditions. It is worth mentioning that this framework can be flexibly extended to other DGMs and features for incremental

clustering, while it also holds potential in data augmentation due to its generative modeling capability. These aspects warrant further investigation.

Appendix I: Derivation of the tighter lower bound

According to Eq. (5) and Eq. (8), the KL divergence term in the ELBO can be expressed as:

$$\begin{aligned}
& D_{KL} \left[q(z, c, v, \eta | x, \hat{w}, \phi) \parallel p(z, c, v, \eta | \varpi) \right] \\
&= \mathbb{E}_{q(z, c, v, \eta | x, \hat{w}, \phi)} \left[\log \frac{q(z | x, \phi) q(c, v, \eta | z, \hat{w})}{p(z | c, \eta) p(c, v, \eta | \varpi)} \right] \\
&= \mathbb{E}_{q(z | x, \phi)} \left[\log q(z | x, \phi) \right] - \mathbb{E}_{q(z, c, \eta | x, \hat{w}, \phi)} \left[\log p(z | c, \eta) \right] \\
&\quad + \mathbb{E}_{q(c, v, \eta | \varpi)} \left[\log \frac{q(c, v, \eta | z, \hat{w})}{p(c, v, \eta | \varpi)} \right]
\end{aligned} \tag{A1}$$

As the DPMM is an infinite mixture model, the term $\mathbb{E}_{q(z, c, \eta | x, \hat{w}, \phi)} \left[p(z | c, \eta) \right]$ can be expressed as:

$$\begin{aligned}
& \mathbb{E}_{q(z, c, \eta | x, \hat{w}, \phi)} \left[\log p(z | c, \eta) \right] \\
&= \int_z q(z | x, \phi) \sum_{k=1}^{\infty} q(c = k) \int_{\eta_k} q(\eta_k) \log p(z | \eta_k) d\eta_k dz \\
&= \sum_{k=1}^{\infty} q(c = k) \int_z q(z | x, \phi) \left[\int_{\eta_k} \mathcal{NW}(\eta_k | \hat{\phi}_k) \log \mathcal{N}(z | \eta_k) d\eta_k \right] dz
\end{aligned} \tag{A2}$$

The integration $\int_{\eta_k} \mathcal{NW}(\eta_k | \hat{\phi}_k) \log \mathcal{N}(z | \eta_k) d\eta_k$ is analytically intractable, and an intuitive approach is to approximate it through Monte Carlo integration given as follows:

$$\begin{aligned}
& \mathbb{E}_{q(z, c, \eta | x, \hat{w}, \phi)} \left[\log p(z | c, \eta) \right] \\
&= \sum_{k=1}^{\infty} q(c = k) \int_{z_n} q(z | x, \phi) \left[\int_{\eta_k} \mathcal{NW}(\eta_k | \hat{\phi}_k) \log \mathcal{N}(z | \eta_k) d\eta_k \right] dz \\
&\approx \sum_{k=1}^{\infty} q(c = k) \int_z q(z | x, \phi) \left[\frac{1}{J} \sum_{j=1}^J \log \mathcal{N}(z | \eta_k^{(j)}) \right] dz, \quad \eta_k^{(j)} \sim \mathcal{NW}(\eta_k | \hat{\phi}_k) \\
&= \frac{1}{J} \sum_{j=1}^J \sum_{k=1}^{\infty} q(c = k) \int_z q(z | x, \phi) \log p(z | \eta_k^{(j)}) dz
\end{aligned} \tag{A3}$$

As $\sum_{k=1}^{\infty} q(c=k) = 1$, the KL divergence can be further simplified as:

$$\begin{aligned}
& D_{KL} \left[q(z, c, v, \eta | x, \hat{\boldsymbol{\omega}}, \phi) \parallel p(z, c, v, \eta | \boldsymbol{\omega}) \right] \\
&= \mathbb{E}_{q(z|x, \phi)} \left[\log q(z|x, \phi) \right] - \frac{1}{J} \sum_{j=1}^J \sum_{k=1}^{\infty} q(c=k) \int_z q(z|x, \phi) \log p(z | \eta_k^{(j)}) dz \\
&+ \mathbb{E}_{q(c, v, \eta | z, \hat{\boldsymbol{\omega}})} \left[\log \frac{q(c, v, \eta | z, \hat{\boldsymbol{\omega}})}{p(c, v, \eta | \boldsymbol{\omega})} \right] \\
&= \frac{1}{J} \sum_{j=1}^J \sum_{k=1}^{\infty} q(c=k) \int_z q(z|x, \phi) \log \frac{q(z|x, \phi)}{p(z | \eta_k^{(j)})} dz + \mathbb{E}_{q(c, v, \eta | z, \hat{\boldsymbol{\omega}})} \left[\log \frac{q(c, v, \eta | z, \hat{\boldsymbol{\omega}})}{p(c, v, \eta | \boldsymbol{\omega})} \right] \\
&= \frac{1}{J} \sum_{j=1}^J \sum_{k=1}^{\infty} q(c=k) D_{KL} \left[q(z|x, \phi) \parallel p(z | \eta_k^{(j)}) \right] + \mathbb{E}_{q(c, v, \eta | z, \hat{\boldsymbol{\omega}})} \left[\log \frac{q(c, v, \eta | z, \hat{\boldsymbol{\omega}})}{p(c, v, \eta | \boldsymbol{\omega})} \right]
\end{aligned} \tag{A4}$$

As $q(z|x, \phi) = \mathcal{N}(z | \mu_z, \sigma_z^2 I)$ and $p(z | \eta_k^{(j)}) = \mathcal{N}(z | \mu_k^{(j)}, (\boldsymbol{\Lambda}_k^{(j)})^{-1})$, the KL divergence can be analytically derived. This approach provides an accurate approximation of the variational lower bound when the number of Monte Carlo samples J is sufficiently large, but this comes at the cost of increased computational complexity. As a result, a more efficient approximation approach is proposed.

According to Jensen's inequality [49], it has:

$$\begin{aligned}
& \mathbb{E}_{q(z, c, \eta | x, \hat{\boldsymbol{\omega}}, \phi)} \left[\log p(z | c, \eta) \right] \\
&= \sum_{k=1}^{\infty} q(c=k) \int_z q(z|x, \phi) \mathbb{E}_{q(\eta_k | \hat{\phi}_k)} \left[\log p(z | \eta_k) \right] dz \\
&\leq \sum_{k=1}^{\infty} q(c=k) \int_z q(z|x, \phi) \log \left(\mathbb{E}_{q(\eta_k | \hat{\phi}_k)} \left[p(z | \eta_k) \right] \right) dz \\
&= \sum_{k=1}^{\infty} q(c=k) \int_z q(z|x, \phi) \log \left[t_{\hat{\nu}_k - D + 1} \left(z | \hat{m}_k, \frac{(\hat{\lambda}_k + 1) \hat{\mathbf{W}}_k}{\hat{\lambda}_k (\hat{\nu}_k - D + 1)} \right) \right] dz
\end{aligned} \tag{A5}$$

where $\hat{\phi}_k = \{\hat{m}_k, \hat{\lambda}_k, \hat{\mathbf{W}}_k, \hat{\nu}_k\}$ denotes the parameters of the normal-Wishart distribution;

D is the dimensionality of z ; $t_{\nu}(\cdot)$ is the Student's t distribution derived from the marginalization of the normal-Wishart distribution [50]. Therefore, it has:

$$\begin{aligned}
& D_{KL} \left[q(z, c, v, \eta | x, \hat{\omega}, \phi) \parallel p(z, c, v, \eta | \varpi) \right] \\
& \geq \mathbb{E}_{q(z|x, \phi)} \left[\log q(z|x, \phi) \right] + \mathbb{E}_{q(c, v, \eta | \hat{\omega})} \left[\log \frac{q(c, v, \eta | z, \hat{\omega})}{p(c, v, \eta | \varpi)} \right] \\
& - \sum_{k=1}^{\infty} q(c=k) \int_z q(z|x, \phi) \log \left[t_{\hat{\nu}_k - D + 1} \left(z | \hat{m}_k, \frac{(\hat{\lambda}_k + 1) \hat{W}_k}{\hat{\lambda}_k (\hat{\nu}_k - D + 1)} \right) \right] dz \\
& = \sum_{k=1}^{\infty} q(c=k) D_{KL} \left[q(z|x, \phi) \parallel t_{\hat{\nu}_k - D + 1} \left(z | \hat{m}_k, \frac{(\hat{\lambda}_k + 1) \hat{W}_k}{\hat{\lambda}_k (\hat{\nu}_k - D + 1)} \right) \right] \tag{A6} \\
& + \mathbb{E}_{q(c, v, \eta | \hat{\omega})} \left[\log \frac{q(c, v, \eta | z, \hat{\omega})}{p(c, v, \eta | \varpi)} \right] \\
& \approx \sum_{k=1}^{\infty} q(c=k) D_{KL} \left[q(z|x, \phi) \parallel \mathcal{N} \left(z | \hat{m}_k, (\hat{\lambda}_k \hat{W}_k)^{-1} \right) \right] + \mathbb{E}_{q(c, v, \eta | \hat{\omega})} \left[\log \frac{q(c, v, \eta | z, \hat{\omega})}{p(c, v, \eta | \varpi)} \right]
\end{aligned}$$

Here a Gaussian distribution is used to approximate the Student's t distribution, with its mean and precision matrix set as the expected values of the normal-Wishart distribution, i.e. \hat{m}_k and $\hat{\lambda}_k \hat{W}_k$, thus making the KL divergence analytically tractable. The rationale of this approximation is that the degrees of freedom of the k th Student's t distribution, $\hat{\nu}_k - D + 1$, are proportional to the expected size of the k th component of the DPMM [20], which makes the Student's t distribution approach a Gaussian distribution given suitable prior ν and component size [50].

According to the above analysis, the objective function becomes:

$$\begin{aligned}
\mathcal{L}'(\theta, \phi, \hat{\omega} | x) &= \mathbb{E}_{q(z|x, \phi)} \left[\log p(x|z, \theta) \right] - \mathbb{E}_{q(c, v, \eta | \hat{\omega})} \left[\log \frac{q(c, v, \eta | z, \hat{\omega})}{p(c, v, \eta | \varpi)} \right] \\
& - \sum_{k=1}^{\infty} q(c=k) D_{KL} \left[q(z|x, \phi) \parallel \mathcal{N} \left(z | \hat{m}_k, (\hat{\lambda}_k \hat{W}_k)^{-1} \right) \right] \tag{A7} \\
& \geq \mathbb{E}_{q(z|x, \phi)} \left[\log p(x|z, \theta) \right] - D_{KL} \left[q(z, c, v, \eta | x, \hat{\omega}, \phi) \parallel p(z, c, v, \eta | \varpi) \right] \\
& = \mathcal{L}_{ELBO}(\theta, \phi, \hat{\omega} | x)
\end{aligned}$$

To make the objective a strictly tighter lower bound, the condition $\log p(x) \geq \mathcal{L}'(\theta, \phi, \hat{\omega} | x)$ must be satisfied. According to Jensen's inequality, it has:

$$\begin{aligned}
\log p(x) &= \log \int \frac{p(x, z, c, v, \eta | \varpi, \theta)}{q(z, c, v, \eta | x, \hat{\varpi}, \phi)} q(z, c, v, \eta | x, \hat{\varpi}, \phi) d(z, c, v, \eta) \\
&= \log \mathbb{E}_{q(z, c, v, \eta | x, \hat{\varpi}, \phi)} \left[\frac{p(x|z, \theta) p(c, v, \eta | \varpi)}{q(z, c, v, \eta | x, \hat{\varpi}, \phi)} p(z|c, \eta) \right] \\
&= \log \left(\mathbb{E}_{q(z, c, v, \eta | x, \hat{\varpi}, \phi)} \left[\frac{p(x|z, \theta) p(c, v, \eta | \varpi)}{q(z, c, v, \eta | x, \hat{\varpi}, \phi)} \right] \mathbb{E}_{q(z, c, v, \eta | x, \hat{\varpi}, \phi)} [p(z|c, \eta)] + \right. \\
&\quad \left. \text{cov} \left(\frac{p(x|z, \theta) p(c, v, \eta | \varpi)}{q(z, c, v, \eta | x, \hat{\varpi}, \phi)}, p(z|c, \eta) \right) \right)
\end{aligned} \tag{A8}$$

where $\text{cov}(\bullet)$ is the covariance. If the covariance is positive or neglectable, it has:

$$\begin{aligned}
\log p(x) &\geq \log \mathbb{E}_{q(z, c, v, \eta | x, \hat{\varpi}, \phi)} \left[\frac{p(x|z, \theta) p(c, v, \eta | \varpi)}{q(z, c, v, \eta | x, \hat{\varpi}, \phi)} \right] + \log \mathbb{E}_{q(z, c, v, \eta | x, \hat{\varpi}, \phi)} [p(z|c, \eta)] \\
&\approx \log \mathbb{E}_{q(z, c, v, \eta | x, \hat{\varpi}, \phi)} \left[\frac{p(x|z, \theta) p(c, v, \eta | \varpi)}{q(z, c, v, \eta | x, \hat{\varpi}, \phi)} \right] \\
&\quad + \log \sum_{k=1}^{\infty} q(c=k) \int_z q(z|x, \phi) \mathcal{N} \left(z \mid \hat{m}_k, (\hat{\lambda}_k \hat{W}_k)^{-1} \right) dz \\
&\geq \mathbb{E}_{q(z, c, v, \eta | x, \hat{\varpi}, \phi)} \left[\log \frac{p(x|z, \theta) p(c, v, \eta | \varpi)}{q(z, c, v, \eta | x, \hat{\varpi}, \phi)} \right] \\
&\quad + \sum_{k=1}^{\infty} q(c=k) \int_z q(z|x, \phi) \log \mathcal{N} \left(z \mid \hat{m}_k, (\hat{\lambda}_k \hat{W}_k)^{-1} \right) dz \\
&= \mathcal{L}'(\theta, \phi, \hat{\varpi} | x)
\end{aligned} \tag{A9}$$

Although the relationship between $\frac{p(x|z, \theta) p(c, v, \eta | \varpi)}{q(z, c, v, \eta | x, \hat{\varpi}, \phi)}$ and $p(z|c, \eta)$ is complex

and the sign of their covariance cannot be determined analytically, in practice, given a

sufficiently large amount of training data, the influence of the likelihood on the

posterior tends to dominant over the prior. This reduces the dependency between

$\frac{p(x|z, \theta) p(c, v, \eta | \varpi)}{q(z, c, v, \eta | x, \hat{\varpi}, \phi)}$ and $p(z|c, \eta)$, leading to a neglectable covariance. In this

scenario, $\mathcal{L}'(\theta, \phi, \hat{\varpi} | x)$ can be regarded as a tighter bound to optimize DPVILL. To

make the derivation more rigorous and applicable to cases where training data are

limited, a hyperparameter γ , which is set as $\gamma = 1$ in our experiments, is introduced

to penalize the overestimate of the KL divergence in Eq. (A5) and ensure the objective function remains a valid lower bound on the log marginal likelihood. Consequently, the final lower bound becomes that given in Eq. (11).

Appendix II: Implementation details of DPVIIL in the case studies

For both case studies, we use the same VAE architecture to form DPVIIL, which is composed of fully connected (FC) layers with rectified linear unit (ReLU) activations, and the linear outputs of decoder are directly used as reconstructions without activation node. The structure is presented in Fig. A1, while the key hyperparameters involved in DPVIIL are listed in Table A1.

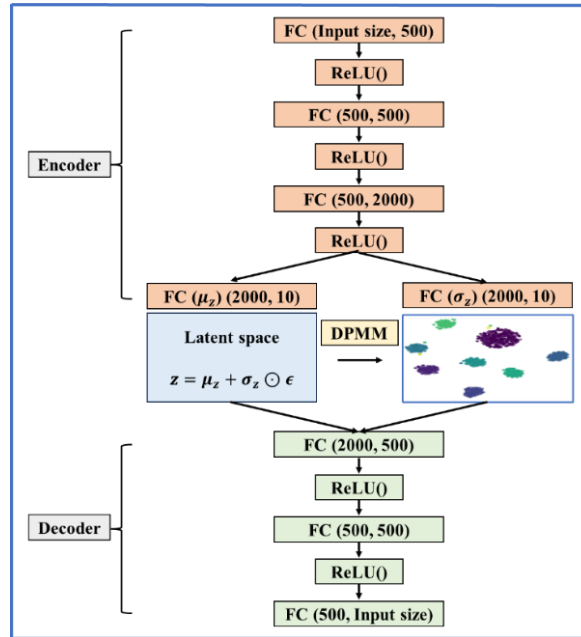


Figure A1. The architecture of DPVIIL used in the case studies.

Table A1. General key hyperparameters of DPVIIL used in the case studies.

Dataset	Numerical shear building	S101 bridge
Optimizer	Adam	Adam
Learning Rate	5e-5	1e-5
Weight Decay	0	0

Train Epochs	150	180
Batch Size	32	16
Concentration parameter	10	10
Penalization factor γ	1	1
Train/Validation/Test Split	0.8/0.1/0.1	0.6/0.2/0.2

Acknowledgements:

This research has been supported by the Science and Technology Development Fund, Macau SAR (File no.: 101/2021/A2, 0038/2024/RIB1, 001/SKL/2024), the Research Committee of University of Macau (File no.: MYRG2022-00096-IOTSC and MYRG-GRG2024-00119-IOTSC), Guangdong-Hong Kong-Macau Joint Laboratory Program (Project No.: 2020B1212030009). Also, the authors highly appreciate VCE for sharing the field test data of S101 Bridge.

Declaration of generative AI and AI-assisted technologies in the writing process

During the preparation of this work the authors used ChatGPT in order to improve the language. After using this tool, the authors reviewed and edited the content as needed and take full responsibility for the content of the publication.

References:

- [1] Farrar, C.R., and Worden, K., *Structural health monitoring: a machine learning perspective*. 2012: John Wiley & Sons.
- [2] Adeagbo, M.O., Wang, S.-M., and Ni, Y.-Q., *Revamping structural health monitoring of advanced rail transit systems: A paradigmatic shift from digital shadows to digital twins*. *Advanced Engineering Informatics*, 2024. **61**: p. 102450.
- [3] Lv, Y., Zhao, W., Zhao, Z., Li, W., and Ng, K.K., *Vibration signal-based early fault prognosis: Status quo and applications*. *Advanced Engineering Informatics*, 2022. **52**: p. 101609.
- [4] Meng, Q., and Zhu, S., *Anomaly detection for construction vibration signals using*

- unsupervised deep learning and cloud computing*. Advanced Engineering Informatics, 2023. **55**: p. 101907.
- [5] Worden, K., Manson, G., and Fieller, N.R., *Damage detection using outlier analysis*. Journal of Sound and Vibration, 2000. **229**(3): p. 647-667.
- [6] Figueiredo, E., Park, G., Farrar, C.R., Worden, K., and Figueiras, J., *Machine learning algorithms for damage detection under operational and environmental variability*. Structural health monitoring, 2011. **10**(6): p. 559-572.
- [7] Yan, W.-J., Chronopoulos, D., Yuen, K.-V., and Zhu, Y.-C., *Structural anomaly detection based on probabilistic distance measures of transmissibility function and statistical threshold selection scheme*. Mechanical Systems and Signal Processing, 2022. **162**: p. 108009.
- [8] Svendsen, B.T., Frøseth, G.T., Øiseth, O., and Rønnquist, A., *A data-based structural health monitoring approach for damage detection in steel bridges using experimental data*. Journal of Civil Structural Health Monitoring, 2022. **12**(1): p. 101-115.
- [9] Mei, L.-F., Yan, W.-J., Yuen, K.-V., and Michael, B., *Structural novelty detection based on Laplace asymptotic expansion of the Bhattacharyya distance of transmissibility function and Bayesian resampling scheme*. Journal of Sound and vibration, 2022: p. 117277.
- [10] Avci, O., Abdeljaber, O., Kiranyaz, S., Hussein, M., Gabbouj, M., and Inman, D.J., *A review of vibration-based damage detection in civil structures: From traditional methods to Machine Learning and Deep Learning applications*. Mechanical Systems and Signal Processing, 2021. **147**: p. 107077.
- [11] Zhang, Y., and Yuen, K.-V., *Review of artificial intelligence-based bridge damage detection*. Advances in Mechanical Engineering, 2022. **14**(9): p. 16878132221122770.
- [12] Flah, M., Nunez, I., Ben Chaabene, W., and Nehdi, M.L., *Machine learning algorithms in civil structural health monitoring: a systematic review*. Archives of Computational Methods in Engineering, 2021. **28**(4): p. 2621-2643.
- [13] Luleci, F., and Catbas, F.N., *A brief introductory review to deep generative models for civil structural health monitoring*. AI in Civil Engineering, 2023. **2**(1): p. 9.
- [14] Ma, X., Lin, Y., Nie, Z., and Ma, H., *Structural damage identification based on unsupervised feature-extraction via variational auto-encoder*. Measurement, 2020. **160**: p. 107811.
- [15] Zhang, L., Wang, B., Liang, P., Yuan, X., and Li, N., *Semi-supervised fault diagnosis of gearbox based on feature pre-extraction mechanism and improved generative adversarial networks under limited labeled samples and noise environment*. Advanced Engineering Informatics, 2023. **58**: p. 102211.
- [16] Yang, X., Yunlei, F., Yuequan, B., and Hui, L., *Few-shot learning for structural health diagnosis of civil infrastructure*. Advanced Engineering Informatics, 2024. **62**: p. 102650.
- [17] Mao, J., Wang, H., and Spencer Jr, B.F., *Toward data anomaly detection for automated structural health monitoring: Exploiting generative adversarial nets and autoencoders*. Structural Health Monitoring, 2021. **20**(4): p. 1609-1626.
- [18] Liu, Y.-S., Yan, W.-J., Yuen, K.-V., and Zhou, W.-H., *Element-wise parallel deep learning for structural distributed damage diagnosis by leveraging physical properties of long-gauge static strain transmissibility under moving loads*. Mechanical Systems and Signal Processing, 2024. **220**: p. 111680.
- [19] Luo, Y., Guo, X., Wang, L.-k., Zheng, J.-l., Liu, J.-l., and Liao, F.-y., *Unsupervised structural*

- damage detection based on an improved generative adversarial network and cloud model*. Journal of Low Frequency Noise, Vibration and Active Control, 2023. **42**(3): p. 1501-1518.
- [20] Mei, L.-F., Yan, W.-J., Yuen, K.-V., and Beer, M., *Streaming variational inference-empowered Bayesian nonparametric clustering for online structural damage detection with transmissibility function*. Mechanical Systems and Signal Processing, 2025. **222**: p. 111767.
- [21] Rogers, T., Worden, K., Fuentes, R., Dervilis, N., Tygesen, U., and Cross, E., *A Bayesian non-parametric clustering approach for semi-supervised structural health monitoring*. Mechanical Systems and Signal Processing, 2019. **119**: p. 100-119.
- [22] Li, Y., Minh, H.-L., Khatir, S., Sang-To, T., Cuong-Le, T., MaoSen, C., and Wahab, M.A., *Structure damage identification in dams using sparse polynomial chaos expansion combined with hybrid K-means clustering optimizer and genetic algorithm*. Engineering Structures, 2023. **283**: p. 115891.
- [23] Zhang, X., Wang, Z., Zhao, D., Wang, J., and Li, Z., *Unsupervised structural damage identification based on covariance matrix and deep clustering*. The Structural Design of Tall and Special Buildings, 2024: p. e2115.
- [24] Mei, L.-F., Yan, W.-J., Yuen, K.-V., Ren, W.-X., and Beer, M., *Transmissibility-based damage detection with hierarchical clustering enhanced by multivariate probabilistic distance accommodating uncertainty and correlation*. Mechanical Systems and Signal Processing, 2023. **203**: p. 110702.
- [25] Sokołowski, J., Obuchowski, J., Wyłomańska, A., Kruczek, P., and Zimroz, R., *Multiple local damage detection method based on time-frequency representation and agglomerative hierarchical clustering of temporary spectral content*. Applied Acoustics, 2019. **147**: p. 44-55.
- [26] Li, S., Laima, S., and Li, H., *Cluster analysis of winds and wind-induced vibrations on a long-span bridge based on long-term field monitoring data*. Engineering Structures, 2017. **138**: p. 245-259.
- [27] Mei, L.-F., Yan, W.-J., Yuen, K.-V., and Beer, M., *Structural novelty detection based on Laplace asymptotic expansion of the Bhattacharyya distance of transmissibility function and Bayesian resampling scheme*. Journal of Sound and Vibration, 2022: p. 117277.
- [28] WEI, S., LI, S., and Li, H., *Clustering of vehicular cable tension of cable-stayed bridge under normal operation conditions*. Structural Health Monitoring 2015, 2015.
- [29] Hu, X., and Xu, L., *Investigation on several model selection criteria for determining the number of cluster*. Neural Information Processing-Letters and Reviews, 2004. **4**(1): p. 1-10.
- [30] Sharma, A., *A note on batch and incremental learnability*. Journal of Computer and System Sciences, 1998. **56**(3): p. 272-276.
- [31] Rezende, D., and Mohamed, S. *Variational inference with normalizing flows*. in *International conference on machine learning*. 2015. PMLR.
- [32] Jiang, Z., Zheng, Y., Tan, H., Tang, B., and Zhou, H., *Variational deep embedding: An unsupervised and generative approach to clustering*. arXiv preprint arXiv:1611.05148, 2016.
- [33] Yang, L., Cheung, N.-M., Li, J., and Fang, J. *Deep clustering by gaussian mixture variational*

- autoencoders with graph embedding.* in *Proceedings of the IEEE/CVF international conference on computer vision.* 2019.
- [34] Ben-Yosef, M., and Weinshall, D., *Gaussian mixture generative adversarial networks for diverse datasets, and the unsupervised clustering of images.* arXiv preprint arXiv:1808.10356, 2018.
- [35] Xie, J., Girshick, R., and Farhadi, A. *Unsupervised deep embedding for clustering analysis.* in *International conference on machine learning.* 2016. PMLR.
- [36] Zhou, S., Xu, H., Zheng, Z., Chen, J., Bu, J., Wu, J., Wang, X., Zhu, W., and Ester, M., *A comprehensive survey on deep clustering: Taxonomy, challenges, and future directions.* arXiv preprint arXiv:2206.07579, 2022.
- [37] Nalisnick, E., and Smyth, P., *Stick-breaking variational autoencoders.* arXiv preprint arXiv:1605.06197, 2016.
- [38] Bing, Z., Meng, Y., Yun, Y., Su, H., Su, X., Huang, K., and Knoll, A., *DIVA: A Dirichlet process mixtures based incremental deep clustering algorithm via variational auto-encoder.* arXiv preprint arXiv:2305.14067, 2023.
- [39] Hughes, M.C., and Sudderth, E., *Memoized online variational inference for Dirichlet process mixture models.* Advances in neural information processing systems, 2013. **26**.
- [40] Teh, Y.W., *Dirichlet Process.* Encyclopedia of machine learning, 2010. **1063**: p. 280-287.
- [41] Blei, D.M., and Jordan, M.I., *Variational inference for Dirichlet process mixtures.* Bayesian analysis, 2006. **1**(1): p. 121-143.
- [42] Kurihara, K., Welling, M., and Vlassis, N., *Accelerated variational Dirichlet process mixtures.* Advances in neural information processing systems, 2006. **19**.
- [43] Kingma, D.P., and Welling, M., *Auto-encoding variational bayes.* arXiv preprint arXiv:1312.6114, 2013.
- [44] Yang, Y., *Temporal data mining via unsupervised ensemble learning.* 2016: Elsevier.
- [45] Döhler, M., Hille, F., Mevel, L., and Rücker, W., *Structural health monitoring with statistical methods during progressive damage test of S101 Bridge.* Engineering Structures, 2014. **69**: p. 183-193.
- [46] Van de Ven, G.M., Tuytelaars, T., and Tolias, A.S., *Three types of incremental learning.* Nature Machine Intelligence, 2022. **4**(12): p. 1185-1197.
- [47] Van der Maaten, L., and Hinton, G., *Visualizing data using t-SNE.* Journal of machine learning research, 2008. **9**(11).
- [48] Liao, L., Li, H., Shang, W., and Ma, L., *An empirical study of the impact of hyperparameter tuning and model optimization on the performance properties of deep neural networks.* ACM Transactions on Software Engineering and Methodology (TOSEM), 2022. **31**(3): p. 1-40.
- [49] Jordan, M.I., Ghahramani, Z., Jaakkola, T.S., and Saul, L.K., *An introduction to variational methods for graphical models.* Machine Learning, 1999. **37**: p. 183-233.
- [50] Murphy, K.P., *Conjugate Bayesian analysis of the Gaussian distribution.* def, 2007. **1**(2 σ 2): p. 16.